# The Life Cycle of a Cyclone Wave in the Southern Hemisphere. Part I: Eddy Energy Budget

I. ORLANSKI AND J. KATZFEY

*Geophysical Fluid Dynamics Laboratory/NOAA, Princeton University, Princeton, New Jersey*

## ABSTRACT

The energetics of a Southern Hemisphere cyclone wave have been analyzed using ECMWF data and the results of a limited-area model simulation. An analysis of the energy budget for a storm that developed in the eastern Pacific on 4–6 September 1987 showed the advection of the geopotential height field by the ageostrophic wind to be both a significant source and the primary sink of eddy kinetic energy. Air flowing through the wave gained kinetic energy via this term as it approached the energy maximum and then lost it upon exiting. Energy removal by diffusion, friction, and Reynolds stresses was found to be small. The most important conclusion was that, while the wave grew initially by poleward advection of heat as expected from baroclinic theory, the system evolved only up to the point where this source of eddy energy and the conversion of eddy potential to eddy kinetic energy (typically denoted "$\omega\alpha$") was compensated for by energy flux divergence (dispersion of energy), mainly of the ageostrophic geopotential flux, $v_a \phi$. Energy exported in this fashion was then available for the downstream development of a secondary system. This finding seems to differ from the results of studies of the life cycle of normal-mode–type waves in zonal flows, which have been shown to decay primarily through transfer of energy to the mean flow via Reynolds stresses. However, this apparent inconsistency can be explained by the fact that while ageostrophic geopotential fluxes can also be very large in the case of individual normal modes, the waves export energy downstream at exactly the same rate as they gain from upstream. The group velocity of the 4–6 September storm, calculated from the ageostrophic geopotential height fluxes, showed that the energy packet comprising the system had an eastward group velocity slightly larger than the time-mean flow.

## 1. Introduction

Strong spring cyclones are common over the open ocean in the Southern Hemisphere, occurring in several identifiable active baroclinic zones and accompanied by large poleward fluxes of heat. Because of the absence of complicating factors such as topography and land–sea contrasts, a detailed analysis of these storms could provide an opportunity to study the life cycle and energetics of wave disturbances from a more nearly idealized standpoint, particularly in terms of wave activity and the advection, conversion, and radiation of wave energy. In early September 1987, a storm over the South Pacific Ocean developed rapidly into a deep cyclone on the periphery of Antarctica and was so intense that the upward transport of low-ozone air to the tropopause on the eastern side of the trough produced a very pronounced ozone minimum at that level over the Palmer Peninsula (Orlanski et al. 1989). Orlanski et al. (1991; hereafter referred to as OKMM) discussed the cyclogenesis that occurred when a disturbance in the subtropics merged with a wave in the polar west-

erlies. As the storm intensified, the subtropical and polar jets merged, creating some poleward heat transports. OKMM described this storm using a high-resolution limited-area numerical simulation and suggested that both barotropic and baroclinic processes were important for development. In the present paper, the relative importance of these processes in the life cycle of a Southern Hemisphere cyclone wave is investigated.

Since the classical works by Charney (1947), Eady (1949), and Kuo (1949) on the development of planetary waves and the growth of cyclone-scale disturbances by baroclinic and barotropic instabilities of the zonal flow, our understanding of the development of these systems has improved greatly. Although comparison with the observed development of large-scale midlatitude disturbances has unquestionably singled out baroclinic processes as the most important mechanism in the generation of cyclonic disturbances, considerable quantitative differences remain between the flows that are observed and the idealized flows used in theoretical studies. More recently, zonal asymmetries in the stability of mean flows (e.g., Simmons et al. 1983; Frederiksen 1983), interaction of upper-tropospheric potential vorticity anomalies with preexisting low-tropospheric cyclones (Hoskins et al. 1985), and the destabilization of the flow by surface fluxes (Or-

*Corresponding author address:* Isidoro Orlanski, Geophysical Fluid Dynamics Laboratory, Forrestal Campus, Princeton, NJ 08542.

lanski 1986) have been considered as factors enhancing development. However, as these local forcings become important for the development of waves or cyclone disturbances, the notion of separation between the disturbance and the mean flow becomes less precise.

The energy conversions that are responsible for the development or decay of cyclone waves in the Northern Hemisphere have been discussed by Simmons (1972), Gall (1976b), and Simmons and Hoskins (1978), among others, for zonal mean flows characteristic of winter conditions for the Northern Hemisphere. Simmons and Hoskins (1978) performed a comprehensive extension of previous works by studying the time evolution of some of the unstable waves (mainly wavenumbers 6 and 9) within different zonal mean flows. Their findings indicate that all the waves are baroclinically unstable, that the nonlinear regime differs substantially from the linear evolution, and that the amplitude of the waves is larger at higher levels than at lower levels. The observational studies of Oort and Ramusson (1971) and Newell et al. (1974) show that the meridional heat and momentum fluxes for the planetary waves in the nonlinear regime tend to have a secondary maximum in the upper troposphere. These studies also indicate that barotropic processes play a major role in the decay of the wave energy after the system occludes.

Kung (1977) analyzed a large number of synoptic cases over a period of five years to determine the important local energy transfers. He found that while cyclones developed through baroclinic energy conversion, some of the eddy energy generated was transported to neighboring regions, contributing to secondary development. No estimate was made of barotropic energy conversion. More recent studies of the Southern Hemisphere (Trenberth 1981; Randel et al. 1987) suggest that some planetary waves may grow due to barotropic instability of the mean flow. Trenberth (1986a,b) suggests that, in particular, the dual jet structure in the · Southern Hemisphere troposphere can be barotropically unstable. He found that strong fluxes of westerly momentum out of the polar flank of the subtropical jet contribute substantially to the growth of eddies by barotropic processes. Simmons et al. (1983) showed that much of the low-frequency variability of the Northern Hemisphere flow could be explained by zonally asymmetric mean flows that are barotropically unstable and that, in localized regions, the instantaneous growth rates of barotropically unstable waves are comparable to those of baroclinically unstable waves.

Although the aforementioned studies indicate that both barotropic and baroclinic processes may be important for the development of waves on the planetary to cyclone scale, the relative importance of these processes for the more transient high wavenumbers has not been demonstrated. Most high-wavenumber, high-frequency waves have the characteristic of developing in localized regions over the globe. Sometimes these short waves can grow at the expense of a decaying system upstream. This downstream development of baroclinic Rossby waves traveling as a time-dependent packet has received very little attention from the theoretical standpoint (Merkine 1977; Simmons and Hoskins 1979; Farrell 1982; Pierrehumbert 1984; Orlanski 1986). Specific examples of downstream effects in the development of storms over the Pacific Ocean may be found in the work of Namias and Clapp (1944), Cressman (1948), Petterssen (1956, p. 356), and Miles (1959). The theoretical interpretation of these observations is based on the idea of atmospheric energy dispersion (Rossby 1945; Yeh 1949) and involves the study of the response of a barotropic fluid to a local source of vorticity. The eastward group velocity of Rossby waves results in the downstream development of a succession of troughs and ridges with time and space scales in broad agreement with those observations.

Simmons and Hoskins (1979) examined the response of a baroclinically unstable atmosphere to a localized initial perturbation using the nonlinear primitive equations on a sphere. They found that the initial disturbance moved downstream, while smaller-scale disturbances developed upstream at the same longitude as the initial disturbance. It was also found that the growth rate was much larger than that of the modal case, with the upper-level amplitude larger than the nonlinear mode calculations. In the nonlinear examples, wave growth ceased before the normal-mode form was established. The downstream length scales were about 30% longer and upper-level amplitudes were generally larger than those found in integrations using normal-mode initial conditions. Using normal-mode initial conditions, Gall (1976) and Simmons and Hoskins (1978) suggested that growth was limited by significant stabilization of the zonal-mean state at low levels, with the upper-level growth ceasing somewhat later than the surface growth. However, in the downstream development case, Simmons and Hoskins (1979) found that the upper-level maximum was reached earlier than the surface maximum, suggesting that either some other form of nonlinearity or the downstream dispersion of energy was limiting the upper-level amplitudes. Observed cyclone waves seem to resemble more closely the downstream development mode of evolution than the nonlinear normal-mode evolution. However, the energetics of such developments are less well understood.

Determination of the processes acting during the complete life cycle of a cyclone wave in the Northern Hemisphere is difficult due to the fact that land–sea contrasts and orographic disturbances constitute a highly asymmetric environment in which the wave grows. However, the southern Pacific Ocean may provide an environment that is more suitable for the study of the evolution of these waves. In fact, the regularity of the eastward-progressing cyclone waves in this region

has been compared with structures observed in laboratory annulus experiments (Randel et al. 1987).

The development of a Southern Hemisphere cyclone wave that occurred in early September 1987 in the South Pacific is analyzed in this paper in an attempt to identify the main processes that controlled its growth and decay. A description of the rapid deepening phase of the wave and its structure was presented in OKMM, in which it was determined that surface fluxes and topography were not important for the development, that the storm had a large barotropic component (i.e., small vertical tilt), and that the wave intensified as the mid-latitude and polar westerlies merged. Here the relation of this storm to the planetary flow is analyzed using deviations from the monthly mean in order to determine the dynamical processes associated with the development. This approach of analyzing the deviation from the time mean in order to investigate the evolution of storm systems has two principal benefits: 1) the removal of the time mean accentuates the important variations of the system and permits the application of a well-developed framework for the analysis of eddy statistics, and 2) the evolutionary characteristics of individual cases can help in interpreting the characteristics of ensembles of waves in the more general study of storm tracks.

The evolution of the September 1987 cyclone wave is analyzed in section 2 using the 30-day mean and time deviations calculated from ECMWF analyses. The regional evolution of the wave and the kinetic energy budget are presented in section 3 using a limited-area model simulation. In section 4, the eddy available potential energy budget and the ageostrophic geopotential fluxes are discussed. The conclusions are presented in section 5.

## 2. Evolution of the cyclone wave in the South Pacific

The development of the wave can be seen in Fig. 1, which shows the time sequence of 500-mb geopotential heights from 1200 UTC 2 September 1987 (hereafter, times and date will be given as 12Z/2) through 1200 UTC 7 September 1987. (The term "wave" is used loosely here, meaning the consecutive ridge and trough of the perturbed geopotential height field and not, as is more commonly used, a spectral component.) A large ridge developed into a closed high at 50°S, 150°W over the first three days and then propagated eastward. The trough associated with the storm deepened east of the ridge near 110°W on 4 September, moved eastward, and began weakening on 7 September (see, in particular, the shaded 5280-m to 5340-m geopotential band). In contrast to the ridge, which extended from the subtropics to middle latitudes, the trough extended from middle to high latitudes. From the point of view of wave development, the trough and ridge were part of a single entity. However, zonal asymmetries, interactions with other waves, and different latitudinal development can locally change the evolution of different parts of the wave. The role that such regional asymmetries may have played in the development of the wave are now addressed in greater detail.

Analysis of the potential vorticity is helpful in clarifying the origin and interaction of the potential vorticity anomaly associated with this cyclone system, particularly at the earlier time periods. ECMWF analyses have been used to compute the potential vorticity,

$$PV = -g\left(\frac{\partial p}{\partial \theta}\right)^{-1}(\zeta + f),$$

and the velocity vectors on the 320 $K$ isentropic surface. Note that PV is negative in the Southern Hemisphere, with higher magnitudes in the polar latitudes being indicative of the 320 K surface lying nearer to or within the stratosphere. The results are shown in Fig. 2 at 12-h intervals from 00Z/3 to 12Z/6 September. The domain has been centered approximately on the area of most rapid evolution of the wave for that period (20°S to 80°S and from 180°W to 0°). Three bands of PV have been shaded in order to highlight the subtropical and high latitude PV. The evolution of the western high (with low magnitude, negative PV) is readily identifiable, but equally important is the large intrusion of low magnitude PV from the subtropics to the sub-Antarctic region at around 90°W after 12Z/4. This subtropical potential vorticity was advected poleward ahead of an eastward-moving high-latitude wave and its associated subpolar potential vorticity maximum (in magnitude). The low-magnitude PV values from the subtropics became trapped in the anticyclonic circulation of the ridge downstream from the high latitude wave. The sequence of events depicted in Fig. 2 shows the general life cycle of a cyclone system in which the initial state, characterized by a rather zonal field with mainly meridional gradients of PV, becomes progressively more contorted, with large intrusions of PV anomalies from the subtropics and subpolar regions.

One characteristic frequently used to detect potential barotropic or baroclinic instabilities in zonal flows is a change in the sign of the meridional gradient of the potential vorticity (Charney and Stern 1962). It should be obvious from Fig. 2 that strong reversals occurred. Figure 3 shows the zonal average for 00Z/3 and 12Z/6 over the sector from 118°W to 31°W (the region where the maximum strengthening occurred) of the zonal wind, the potential temperature, the Ertel potential vorticity, and the meridional gradient of potential vorticity on isentropic surfaces (negative $\partial PV/\partial y$ is shaded). In this sector, there was indeed a large vertical zone of negative meridional gradients of potential vorticity. However, it is the strong baroclinic evolution that took place between 00Z/3 and 12Z/6 that is most apparent, evident in the reduction of the slopes of potential temperatures and the decrease in the vertical wind shear (see upper and lower left panels). The flow
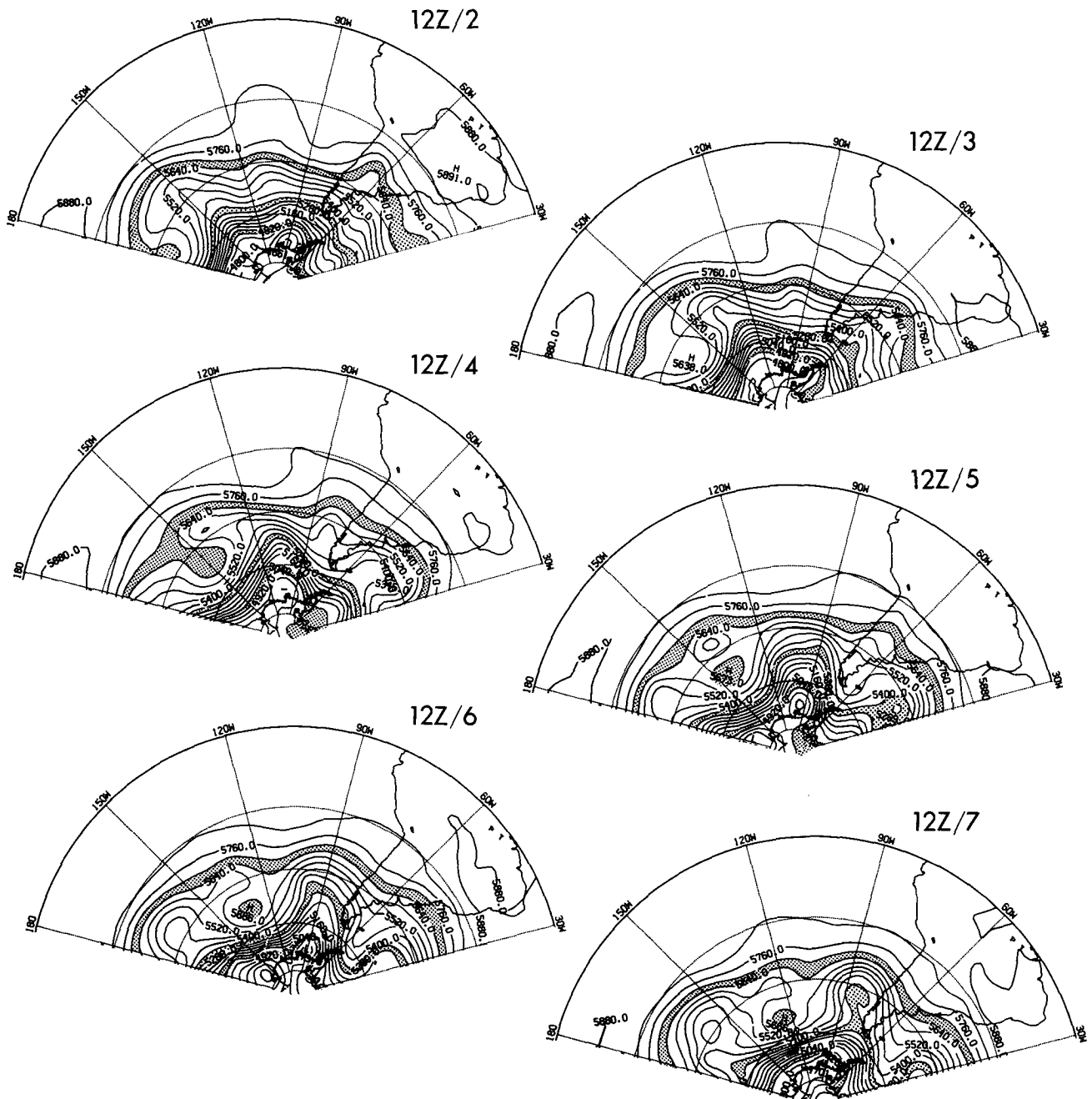
## 500mb GEOPOTENTIAL HEIGHTS

FIG. 1. 500-mb geopotential heights at 1200 UTC 2–7 September. Contour interval: 60 m, shaded between 5700 and 5640 m and between 5340 and 5280 m. Latitude circles are drawn every 20°.

field also changed dramatically, with the development of weak winds and vertical shears in the midlatitudes (around 50°S) and strong shears at either side. This change in the environment from a wide baroclinic zone at 00Z/3 (Fig. 3 upper left) to a weak baroclinic zone flanked by two strong baroclinic zones at 12Z/6 (Fig. 3 lower left) seems to confirm findings by Simmons and Hoskins (1978) and Nakamura (1988) that baroclinic development, while reducing the mean baroclinicity, enhances baroclinicity to either side of the dis-
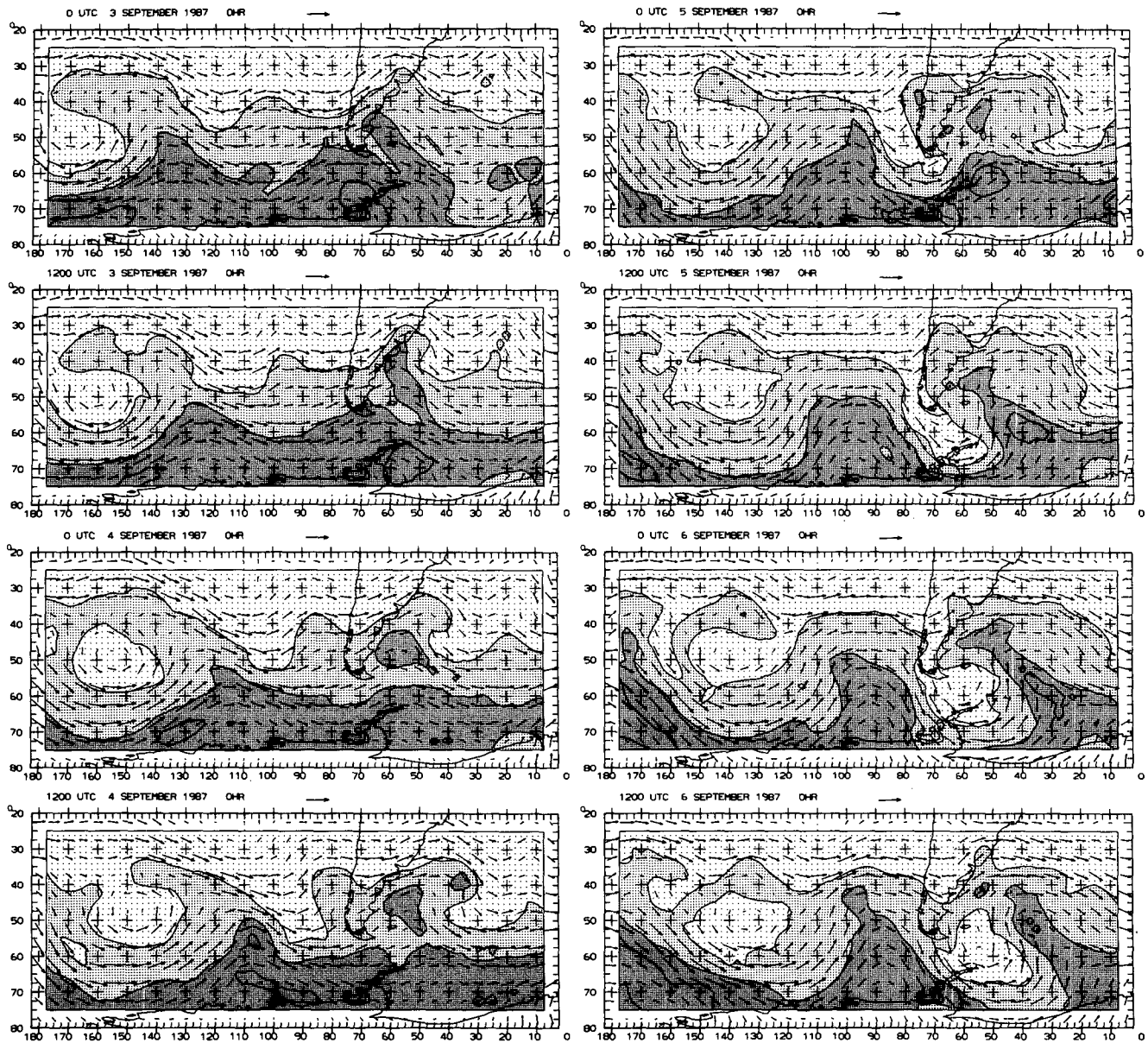
ERTEL PV ON 320°K ISENTROPIC SURFACE



FIG. 2. Potential vorticity and wind vectors on the 320 K isentropic surface (approximately 250 hPa at 50°S) at 12-h intervals, from 0000 UTC 3 September to 1200 UTC 6 September. Dark, medium, and light shading correspond to regions of less than $-4 \times 10^{-6}$ m$^2$ K s$^{-1}$ kg$^{-1}$, $-4$ to $-2 \times 10^{-6}$ m$^2$ K s$^{-1}$ kg$^{-1}$, and greater than $-2 \times 10^{-6}$ m$^2$ K s$^{-1}$ kg$^{-1}$, respectively. Arrow at top of panel indicates wind speed of 10 m s$^{-1}$.

turbance. However, there is a fundamental difference between our final state and these previous studies. Whereas baroclinic instability tends to enhance the mean barotropic flow as shown in Gill (1982, p. 579), the flow in this case produced a zonal wind minimum rather than a barotropic jet.

A comparison of the sector-averaged potential vorticity (right panels of Fig. 3) also suggests a significant modification of the mean flow by the evolving wave, with latitudinal spreading of low magnitude PV over

the time period indicating considerable PV mixing. However, there continue to be PV gradient reversals, so that the necessary condition for instability remains. In addition, the poleward motion of the storm has kept it in a region of high baroclinicity. Together, these conditions suggest that the actual decay of the system cannot necessarily be attributed to the stabilization of the mean flow. As will be shown later, other processes such as dispersion of energy to other systems could also play a very important role in its decay. In addition, given
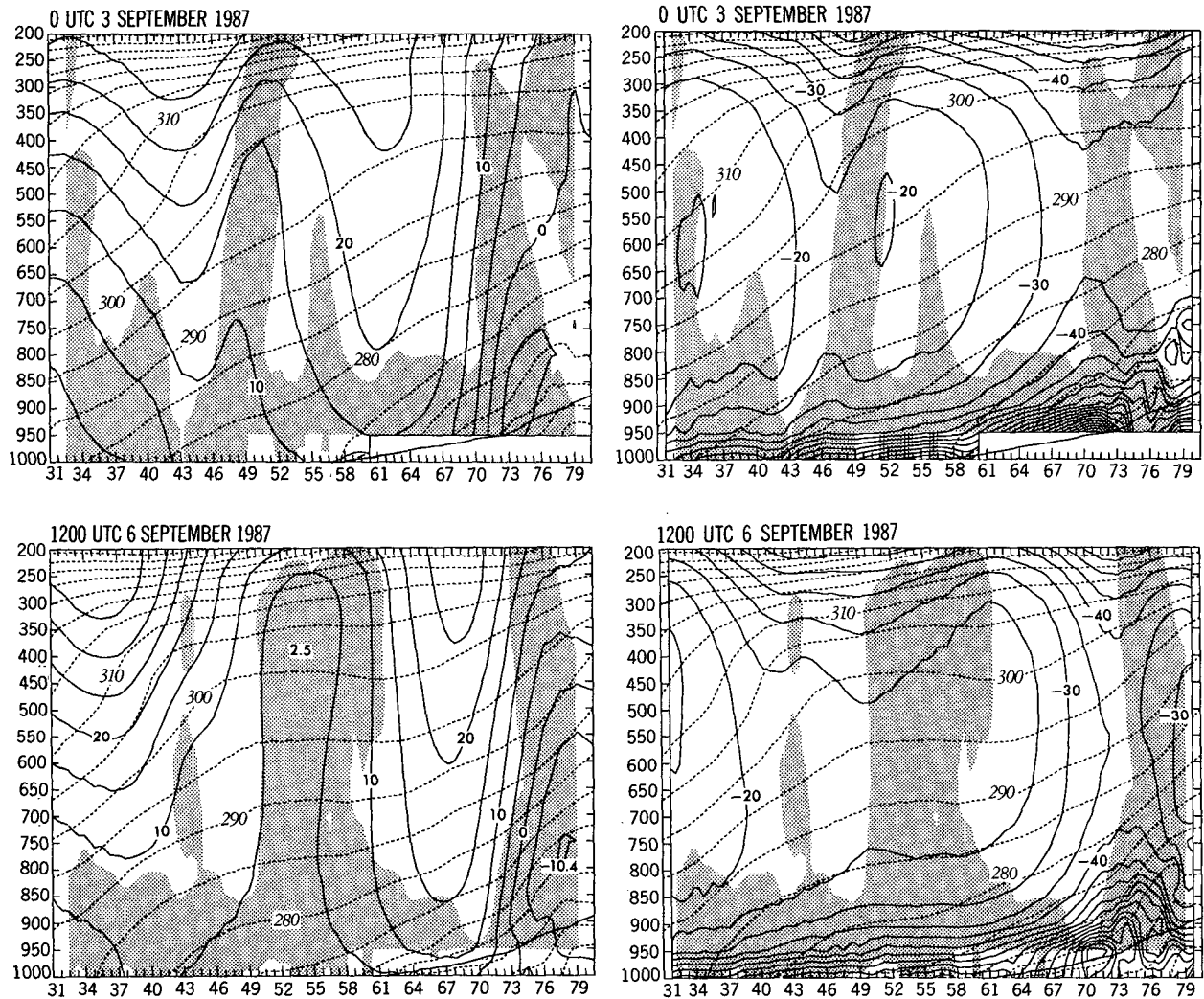
## SECTOR ZONAL AVERAGE U,θ, ERTEL–PV



FIG. 3. Left panels: sector average (118°–31°W) of potential temperature (dashed, every 5 K), zonal wind (solid, every 5 m s⁻¹), and negative meridional potential vorticity gradients (shaded) for 0000 UTC 3 September (bottom) and 1200 UTC 6 September (top). Right panels: same as left panels except solid lines are potential vorticity (interval: $5 \times 10^{-6}$ m² K s⁻¹ kg⁻¹).

that PV gradient reversals and low-level temperature gradients remain, subsequent baroclinic development cannot be ruled out.

Thus far, we have described the 3–6 September 1987 South Pacific cyclone only in terms of the time evolution of the geopotential and potential vorticity fields. In order to fully understand the development of the system within the time-mean flow and to gain insight into the wave–mean flow interaction for this particular storm, we will now address the energy budget as it applies to an individual system.

### 3. Eddy kinetic energy budget

To better identify and isolate the specific cyclone wave that is the focus of this study, the eddy kinetic

energy was calculated every 12 h from 12Z/2 to 12Z/7 September. Figure 4 shows the eddy kinetic energy, $K_e$, versus time for the two principal troughs and the western ridge (see Fig. 1). The $K_e$ of the western ridge increased until 12Z/3 September and decreased thereafter. The $K_e$ of the main trough grew slowly at first and then underwent a rapid increase commencing at around 12Z/4 September. The $K_e$ of this wave reached a maximum 30 h later and decreased rapidly thereafter. The decrease in the $K_e$ of the main trough coincided with an increase in the $K_e$ of the eastern trough (located at 30°W on 12Z/5—see Fig. 1). This pattern suggests an eastward propagation of energy in which each phenomenon intensifies through the influx of energy and decays as the energy radiates downstream. This evolution is investigated in greater detail
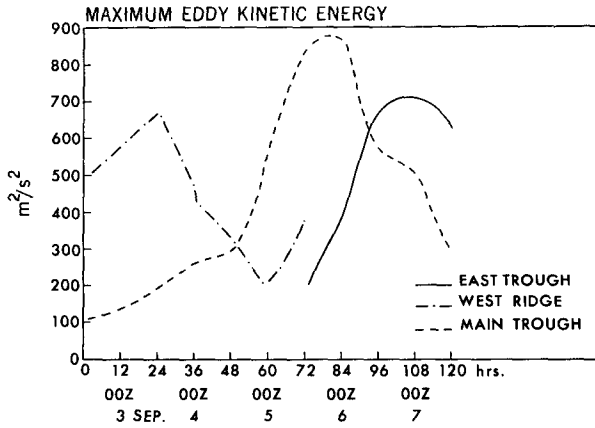
FIG. 4. Vertically averaged maximum eddy kinetic energy for three weather systems in South Pacific.

through the application of the kinetic energy equations that are developed in the next section.

### a. The basic equations

The standard momentum and hydrostatic equations in pressure coordinates can be written as follows (e.g., Haltiner and Williams 1979):

$$\frac{d\mathbf{V}}{dt} + \omega \frac{\partial \mathbf{V}}{\partial p} + f\mathbf{k} \times \mathbf{V} = -\nabla\Phi + \mathbf{Fr} \qquad (3.1)$$

$$\frac{\partial \Phi}{\partial p} = -\alpha, \qquad (3.2)$$

where $\mathbf{V}$ is the two-dimensional horizontal wind velocity, $\omega = dp/dt$ is the vertical velocity in pressure coordinates, $f$ is the Coriolis parameter, $\Phi$ is the geopotential height, $\mathbf{Fr}$ represents the frictional forces, $\alpha$ is the specific volume, and $d/dt$ is defined as $\partial/\partial t + \mathbf{V} \cdot \nabla_p$. The continuity equation in pressure coordinates is

$$\nabla_p \cdot \mathbf{V} + \frac{\partial \omega}{\partial p} = 0. \qquad (3.3)$$

The surface $\omega$ is given by

$$\omega_s = \frac{\partial p_s}{\partial t} + \mathbf{V}_s \cdot \nabla p_s = -\int_0^{p_s} \nabla_p \cdot \mathbf{V} dp, \qquad (3.4)$$

with $p_s$ being the surface pressure. The thermodynamic equation is given by:

$$c_p \frac{dT}{dt} + c_p \omega \frac{\partial T}{\partial p} - \omega\alpha = Q \qquad (3.5)$$

or in terms of the potential temperature $\Theta = T(p_o/p)^\kappa$ as

$$\frac{d\Theta}{dt} + \omega \frac{\partial \Theta}{\partial p} = \frac{Q\Theta}{Tc_p}, \qquad (3.6)$$

where $Q$ represents the rate of heat energy addition by diabatic processes, $p_o$ is a reference pressure (usually 100 kPa), and $\kappa = R/c_p$.

The kinetic energy equation per unit mass is easily obtained by taking the dot product of (3.1) and $\mathbf{V}$. The pressure coordinate form of this equation is

$$\frac{dK}{dt} = \frac{\partial K}{\partial t} + \mathbf{V} \cdot \nabla K + \omega \frac{\partial K}{\partial p} = -\mathbf{V} \cdot \nabla \Phi + \text{diss},$$

$$(3.7)$$

where $K = \frac{1}{2}(U^2 + V^2)$, and diss $= \mathbf{V} \cdot \mathbf{Fr}$ represents the frictional sink.

### b. Partitioning of the kinetic energy equation

Energy budgets are a powerful tool in determining the processes important for the development of weather systems. Scientists, inspired by the predictions of stability theories, have tried to describe the transfer of energy between the mean flow and the planetary scale, as well as to partition the standing and transient eddy activity, based on actual observations. Analyses of this type have also been extended to cyclone waves for idealized baroclinic flows (Simmons 1972; Simmons and Hoskins 1978; Gall 1976). These analyses are based on deviations from zonal or time-mean flows and, as such, require either a large domain for the zonal mean or a long time interval for the time mean. However, statistics based on typical zonal and/or time-mean datasets often include only a handful of weather systems, each of which makes a distinct contribution to the "mean" state. It is important, then, to analyze the energy transfer between an individual, representative weather system and its neighboring systems, as well as the mean flow.

In order to study the time evolution of the energy budget, a system of energy equations must be derived that contains the balance of the time-mean flow, the predictive equation for the first-order kinetic energy time fluctuation, and the eddy kinetic energy. Let us assume that the instantaneous horizontal velocity, $V$, and geopotential fields are given by

$$\mathbf{V} = \mathbf{V}_m + \mathbf{v} \qquad (3.8)$$

$$\Phi = \Phi_m + \phi, \qquad (3.9)$$

where the subscript $m$ indicates the monthly time mean and the small $\mathbf{v}$ and $\phi$ are the deviations from this time mean. The kinetic energy per unit mass will be given by

$$K = \frac{1}{2}\mathbf{V}_m \cdot \mathbf{V}_m + \mathbf{V}_m \cdot \mathbf{v} + \frac{1}{2}\mathbf{v} \cdot \mathbf{v} = K_m + K_1 + K_e,$$

$$(3.10)$$

where $K_m$, $K_1$, and $K_e$ are the kinetic energies for the mean flow, the first-order correlation, and the eddy field, respectively. Of course, the time mean of $K$ will

contain only $K_m$ and the time average of $K_e$, since the time average of $K_1$ is zero. However, $K_1$ could contribute considerably to the energy budget on shorter time scales.

An average circulation calculated for a period as short as one month certainly cannot be considered steady. Therefore, without losing any generality we will assume that the nonsteadiness of the time mean is due to a forcing term, $F_o$. Then

$$\frac{D}{Dt} \mathbf{V}_m = -f\mathbf{k} \times \mathbf{V}_m - \nabla \Phi_m$$

$$+ \, \mathbf{F}r_m - \overline{\mathbf{v} \cdot \nabla \mathbf{v} - \omega \frac{\partial \mathbf{v}}{\partial p}} + \mathbf{F}_o, \quad (3.11)$$

where

$$\frac{D}{Dt} = U_M \frac{\partial}{\partial x} + V \frac{\partial}{\partial y}$$

and $\mathbf{F}r_m$ is the time mean of the frictional forces. Here, the overbar, $\overline{(\ \ )}$, is used to indicate the time mean of terms that are combinations of parameters, so that

$$\overline{-\mathbf{v} \cdot \nabla \mathbf{v} - \omega \frac{\partial \mathbf{v}}{\partial p}}$$

represents the time-mean eddy forcing term. The time-mean flow is assumed to be sufficiently nondivergent so that the vertical motion in (3.11) is entirely attributable to the eddies. Here $\mathbf{F}_o$ can be interpreted as the time average of the local momentum tendency. This will be seen more clearly when discussing the time perturbation equation. The total momentum equation minus the time mean gives the momentum equation for the time deviation

$$\left( \frac{\partial}{\partial t} + U_m \frac{\partial}{\partial x} + V_m \frac{\partial}{\partial y} \right) \mathbf{v} + \mathbf{v} \cdot \nabla \mathbf{V}_m + \omega \frac{\partial \mathbf{V}_m}{\partial p}$$

$$+ \, \mathbf{v} \cdot \nabla \mathbf{v} - \overline{\mathbf{v} \cdot \nabla \mathbf{v}} = -f\mathbf{k} \times \mathbf{v} - \nabla \phi - \omega \frac{\partial \mathbf{v}}{\partial p}$$

$$+ \, \omega \overline{\frac{\partial \mathbf{v}}{\partial p}} + \mathbf{F}r_e - \mathbf{F}_o, \quad (3.12)$$

where $\mathbf{F}r_e$ indicates the difference between the total and the time mean viscous forces. Note that in a time average of (3.12), all terms either go to zero or cancel, with the exception of the local tendency and $\mathbf{F}_o$. Since the time mean of the local tendency of $\mathbf{v}$ is not necessarily zero (because the initial and final $\mathbf{v}$ are not necessarily equal), the local tendency of $\mathbf{v}$ is equal to the change in the total wind and to minus $\mathbf{F}_o$. Therefore, the time mean of (3.12) will be identically satisfied.

The equations for $K_m$ and $K_e$ are obtained by the scalar multiplication of (3.11) by $\mathbf{V}_m$ and (3.12) by $\mathbf{v}$,

respectively. The time-mean kinetic energy equation is given by

$$\mathbf{V}_m \cdot \nabla K_m + \mathbf{V}_m \cdot \overline{\left( \mathbf{v} \cdot \nabla \mathbf{v} + \omega \frac{\partial \mathbf{v}}{\partial p} \right)} + \mathbf{V}_m$$

$$\times \, \nabla \Phi_m + \mathrm{diss}_m - \mathbf{V}_m \cdot \mathbf{F}_o = 0. \quad (3.13)$$

The equation for $K_1$ is considerably more involved than $K_m$ and the derivation is shown in the Appendix. The equation for $K_e$ is given as

$$\frac{\partial K_e}{\partial t} + \mathbf{V}_m \cdot \nabla K_e + \mathbf{v} \cdot \nabla_3 K_e$$

$$= -(\mathbf{v} \cdot \nabla \phi) - (\mathbf{v} \cdot (\mathbf{v} \cdot \nabla_3 \mathbf{V}_m))$$

$$+ \, (\mathbf{v} \cdot \overline{(\mathbf{v} \cdot \nabla_3 \mathbf{v})}) - \mathrm{diss}_e + \mathbf{v} \cdot \mathbf{F}_o. \quad (3.14)$$

The terms on the left of (3.14) are the local tendency, the advection by the mean flow, and the advection by the eddies. The eddy advection is typically assumed to be small in the mean, but it could be as large as the advection by the mean flow for the time-dependent evolution. Note that we have included the vertical component in the advection terms as well.

The first term on the rhs of (3.14) is the pressure work term associated with the eddies, and the fourth term represents dissipation by the eddies. The second term is the energy conversion by the Reynolds stresses which, when properly averaged in time or space, could be interpreted as a transfer between mean and eddy kinetic energy. In the time-dependent evolution, however, the energy transfer is from $K_e$ to $K_1$ and from $K_1$ to $K_m$. The third term on the rhs of (3.14), similar to the previous term, is a net conversion of $K_e$ to $K_1$ and is zero in the time mean sense. Finally, the last term is the effect of the stationary forcing of the mean flow into the eddies. A long time-mean average of this term would be zero, but is negligible even on a shorter time scale since $\mathbf{F}_o$, which is the difference between the total velocities at the initial and final states divided by the time period of the average, is, in the worst case of totally uncorrelated initial and final states, of the order of the velocity itself. Thus,

$$\mathbf{F}_0 = \frac{\Delta \mathbf{v}}{\Delta t} \approx \frac{\mathbf{v}}{\Delta t} \approx \frac{20 \text{ m s}^{-1}}{1 \text{ month}} \approx 1 \times 10^{-5} \text{ m s}^{-2},$$

whereas the local acceleration is at least an order of magnitude larger.

Before presenting the calculated values of the different terms in (3.14), let us define a vertical average as

$$\hat{A} = \frac{1}{(p_s - p_T)} \int_{p_T}^{p_s} A \, dp,$$

where $P_s$ is the surface pressure and $P_t$ is the pressure at the top of the data (100 mb). Unless otherwise stated,

the results will be shown as vertical averages, with the hat dropped for simplicity of notation.

### c. Time evolution of the eddy kinetic energy

A sequence of the vertically averaged eddy kinetic energy, derived from analysis of the ECMWF dataset, is shown in Fig. 5 for 12 h intervals between 00Z/3 and 12Z/6. The domain is the same as in Fig. 2. In order to enhance the regions of larger $K_e$, three different shadings were used, with light shading between 250 and 500 m$^2$ s$^{-2}$, medium shading between 500 and 750 m$^2$ s$^{-2}$, and dark shading for values larger than 750 m$^2$ s$^{-2}$. Individual energy packets are identified by letters.

The time evolution of the different packets of $K_e$ illustrate the different means by which energy is either advected, radiated, or generated and dissipated in situ and is perhaps central to the discussion in this paper. Most of the centers tend to move eastward (about 1° longitude per day or approximately 15 m s$^{-1}$), which is approximately the same as the mean flow at those latitudes. The $K_e$ maxima, although appearing to be isolated packages, may be linked to a given wave, as seen in Fig. 1. For instance, centers A, B, E, and F occur around the western high in the geopotential field. Center D, the most intense center that developed in this period, is colocated with the developing eastern trough of Fig. 1, whereas center C seems to have its origins in a trough that developed over the Andes mountains and center G seems to be connected to development of a secondary trough downstream from the main trough.

The advection of the $K_e$ maxima by the mean flow cannot fully explain the observed eastward propagation of energy. In addition, the poleward translation for some of the centers, particularly C and D, cannot be explained by the primarily eastward mean flow. Since both centers C and D are located on the eastern side of developing troughs, a simple explanation, which will be verified later, is that the advection by the eddies themselves produces this poleward shift.

The "energy packet" approach has been found to provide a better description of the cyclone system than the "wave" concept discussed with respect to Fig. 1, since different parts of the 500-mb geopotential height wave evolve quite independently of each other. In this case, the region of the "wave" between the eastern side of the trough and downstream ridge, where energy center D is located, evolves differently and quite independently from other energy centers associated with the same "wave."

### d. Eddy kinetic energy budget

To better understand the transport, sources, and sinks associated with the $K_e$ patterns shown in Fig. 5, the $K_e$ budget of this cyclone system is analyzed by

applying (3.14) to a numerical simulation made using the limited-area HIBU model described in OKMM. While it may at first seem strange to base such an investigation on a simulation rather than the actual analysis of the observations, one should note that the "analysis" of the observations is, in any case, heavily dependent on model output in data-sparse regions such as the South Pacific. Furthermore, these analyses are typically available only at coarse time resolution. Limited-area model simulations, on the other hand, provide us with internally consistent data, which is of higher resolution in both space and time and permits verification of smaller-scale features via satellite cloud and ozone measurements.

The use of model output in this case was fully justified in light of the high quality of the simulation, which was described by OKMM, who performed a number of limited-area simulations of this cyclone for the period 12Z/4–12Z/6 September 1987. The role of surface processes in the development was investigated and it was found that the development of the storm was not very sensitive to the distribution of landmass or orography, but did show some sensitivity to surface friction effects, evidenced by significant increases in the vertically averaged kinetic energy when the surface roughness was reduced. Surface heat fluxes did not appear to be significant for the intensification of the storm.

For simplicity, we will focus on two specific periods in the storm's evolution to illustrate the role of the various terms in the energy equation (3.14). These periods correspond roughly to the growth (00Z/5) and decay (00Z/6) stages of the wave. The left side of Fig. 6 shows the distribution of eddy kinetic energy $K_e$ for these two periods in the simulation, with the 300 m$^2$ s$^{-2}$ contour enhanced. Note that the maximum $K_e$ at 00Z/5 is 579 m$^2$ s$^{-2}$, increasing to 748 m$^2$ s$^{-2}$ by 00Z/6. On the right of Fig. 6 are the local tendencies, $\partial K_e/\partial t$, calculated as a 6 h time difference centered at the time of interest. The tendencies reflect the eastward and poleward movement of the energy packet. Note that during the period of wave growth, the region of positive tendency has a larger absolute value than the region of negative tendencies, while the opposite situation holds true for the decay stage. A volume integral over the region of maximum $K_e$ (e.g., the area enclosed by the dashed energy contour shown in the left panels) would show the net effect of the tendencies to be positive at 00Z/5 and negative at 00Z/6. The gross behavior of the local tendencies can be explained by the advection of energy by both the mean wind and the eddies. This can be seen in Fig. 7, which shows the advection by the mean winds, $\mathbf{V}_m \cdot \nabla K_e$, on the left, and the advection by the eddies, $\mathbf{v} \cdot \nabla_3 K_e$, on the right. The eastward advection due to the mean flow and the poleward advection by the eddies is clearly evident. Note that the eddy advection of $K_e$, commonly assumed to be a third-order quantity, is of the same order as the mean advection. Integrated over a sufficient

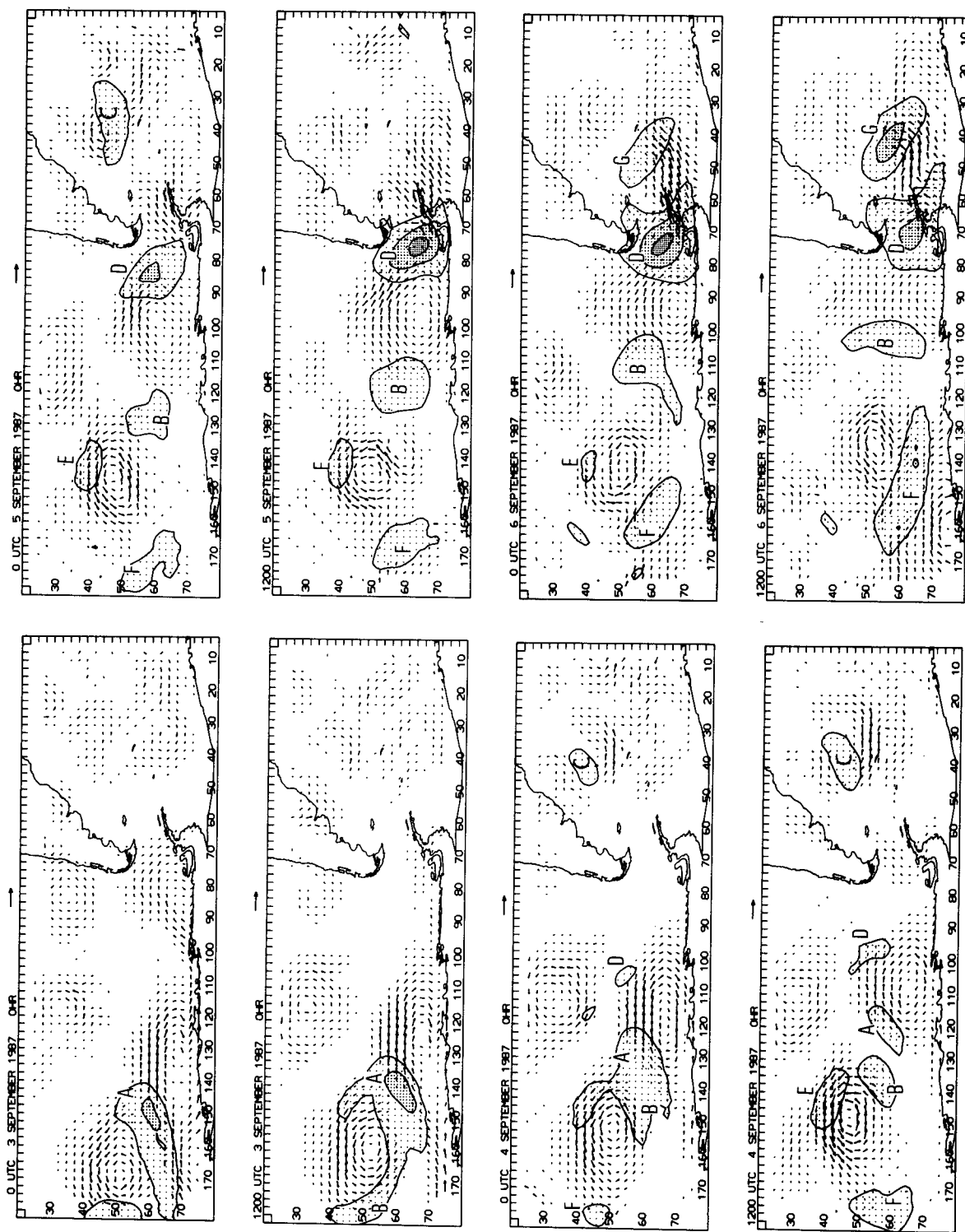EDDY KINETIC ENERGY AND AGEOSTROPHIC GEOPOTENTIAL FLUX



FIG. 5. Vertically averaged eddy kinetic energy and ageostrophic geopotential height flux vectors at 12 h intervals, from 0000 UTC 3 September to 1200 UTC 6 September. Light, medium, and dark shading correspond to kinetic energy values of 250–500 m² s⁻², 500–750 m² s⁻², and greater than 750 m² s⁻², respectively. Flux vectors are in units of 2 × 10⁴ m³ s⁻³ (see arrow above panel).

EDDY KINETIC ENERGY TENDENCY

EDDY KINETIC ENERGY
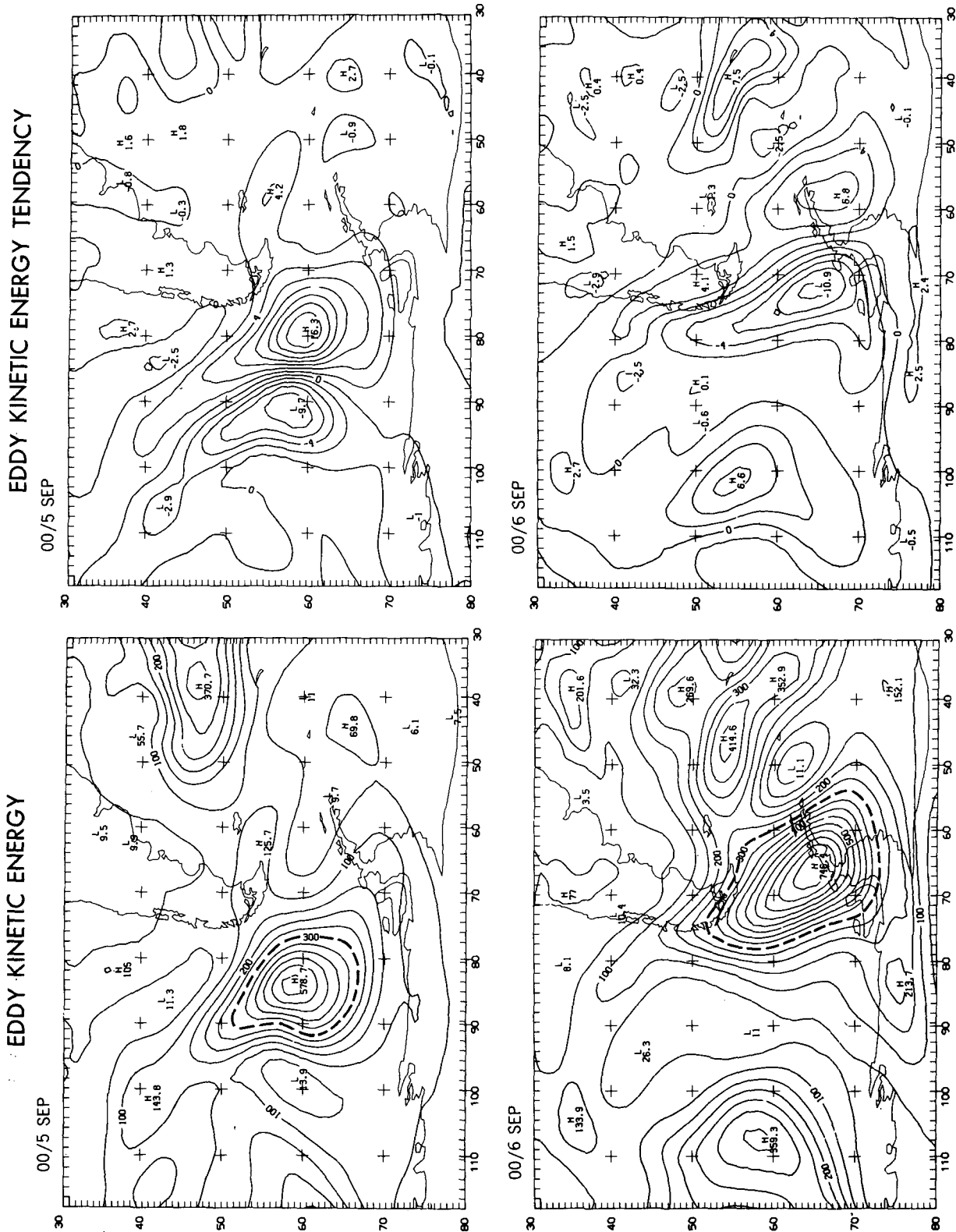
FIG. 6. Vertically averaged eddy kinetic energy (left panels, interval: 50 m$^2$ s$^{-2}$, heavy dashed contour indicates 300 m$^2$ s$^{-2}$) and vertically averaged local tendencies of eddy kinetic energy (right panels, interval: 0.002 m$^2$ s$^{-3}$). Upper and lower graphs correspond to 0000 UTC 5 September and 0000 UTC 6 September, respectively.
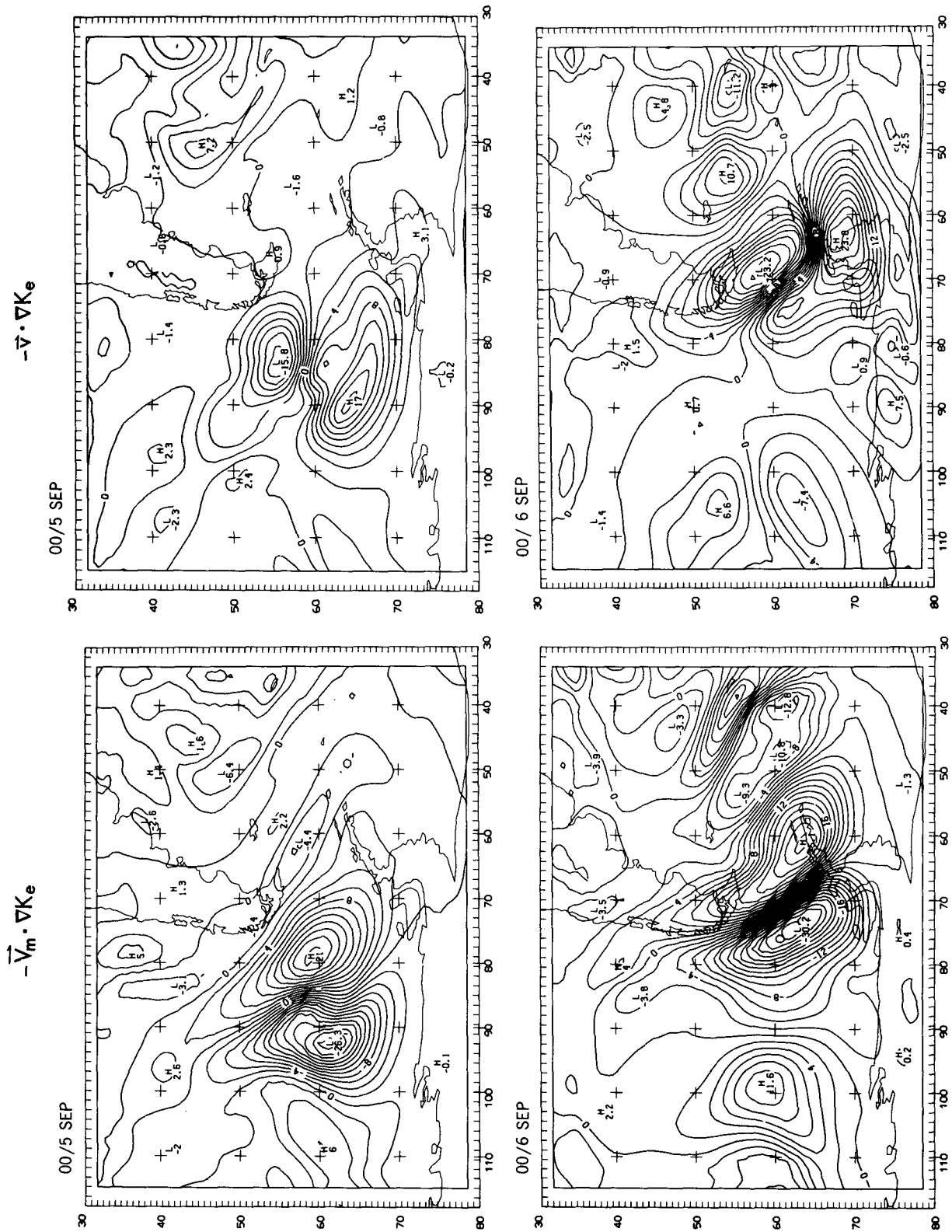
FIG. 7. The vertically averaged eddy kinetic energy advection by the 30-day mean flow (left panels) and by the eddies (right panels), contour interval: 0.002 m² s⁻³. Upper and lower panels correspond to 0000 UTC 5 September and 0000 UTC 6 September, respectively.

length of time, it is likely that the magnitude of the eddy advection term would indeed be smaller than that of the mean wind. However, it is important to point out that while the advection terms dominate the gross behavior of the tendency field, their contributions largely cancel when integrated over a volume containing the entire disturbance, and the *net* tendency/growth is determined more by the remaining terms in (3.14).

Let us now discuss some of the source and sink terms, which appear on the right-hand side of (3.14). The quantity $-\mathbf{v} \cdot \nabla \phi$ is plotted on the left of Fig. 8. This term is positive upstream of the energy packet and negative downstream throughout the life of the system. During the growth stage, the positive values are larger than the negative and, as will be shown later, a volume integral of this term over the region bounded by the 300 m$^2$ s$^{-2}$ $K_e$ contour is positive at this time. During the decay stage, the region of negative tendencies is much more intense and the integral is negative. The distribution of $-\mathbf{v} \cdot \nabla \phi$ relative to the region of maximum $K_e$ makes intuitive sense given that the axis of the local jet is aligned with the positive and negative areas of $-\mathbf{v} \cdot \nabla \phi$. In a Lagrangian sense, the upsteam air gains kinetic energy while flowing through the region of positive $-\mathbf{v} \cdot \nabla \phi$, reaches a maximum near the zero contour, and then loses kinetic energy downstream as it flows through the region of negative $-\mathbf{v} \cdot \nabla \phi$.

The quantities plotted on the right of Fig. 8 represent the conversion of $K_e$ to $K_1$ by the Reynolds stress term, expressed in (3.14) as $-\mathbf{v} \cdot (\mathbf{v} \cdot \nabla_3 \mathbf{V}_m)$. In the time-averaged budget, this term represents the conversion from $K_e$ to $K_m$. At 00Z/5, the values are primarily positive, indicating a slight barotropic contribution to the wave growth, but with smaller magnitudes than the contribution from the $-\mathbf{v} \cdot \nabla \phi$ term. At 00Z/6, the Reynolds stress term is primarily negative, suggesting, as did the Simmons and Hoskins (1978) study of the nonlinear life cycle of a cyclone wave, that eddy kinetic energy decays via transfer of energy to the mean flow. However, it should be pointed out that, in this case, this term is rather small and cannot by itself explain the decay of $K_e$.

The remaining terms on the rhs of (3.14) could not be calculated directly, but are expected to be rather small. It was, however, possible to calculate the *total* dissipation (as opposed to eddy dissipation alone), which is shown in Fig. 9. While it is likely that the local dissipation due to the eddy field would dominate that of the mean flow, even the total dissipation was found to be rather small [on the order of $(-1$ to $-4) \times 10^{-3}$ m$^2$ s$^{-3}$] when compared to the other terms in (3.14).

### e. Ageostrophic geopotential fluxes

It was shown in the previous section that $-\mathbf{v} \cdot \nabla \phi$ is the dominant source term in the local eddy kinetic energy budget. A more thorough discussion of the re-

lation of this term to the ageostrophic geopotential fluxes and $\omega \alpha$ is now presented.

The ageostrophic geopotential eddy flux can be defined, without losing any generality, as

$$\mathbf{v}_a \phi = \left( \mathbf{v} - \frac{\mathbf{k}}{f_o} \times \nabla \phi \right) \phi, \qquad (3.15)$$

where $\mathbf{v}_a$ is the ageostrophic velocity relative to the geostrophic flow at a reference latitude with Coriolis force $f_o$. Note that the divergence of the vector on the left side of (3.15) is equal to the divergence of the total flux, $\mathbf{v}\phi$, since the second term in the parentheses represents the flux by the geostrophic flow, which is nondivergent. The ageostrophic geopotential flux vectors shown in Fig. 8 are superimposed on the field of $-\mathbf{v} \cdot \nabla \phi$. The correlation between the region of ageostrophic geopotential flux divergence and the region of negative $-\mathbf{v} \cdot \nabla \phi$ is readily apparent. The vertically averaged $-\mathbf{v} \cdot \nabla \phi$ is equal to

$$-\mathbf{v} \cdot \nabla \phi = -(\nabla \cdot (\mathbf{v}\phi)) - \omega \alpha - \frac{\omega \phi |_{p_t}^{p_s}}{(p_s - p_t)}. \qquad (3.16)$$

For small amplitude waves, the quantity $\mathbf{v}\phi$ represents an energy flux, which will be referred to as a "radiative" energy flux to distinguish it from the advective part. The last term on the rhs of (3.16) is negligible because $\omega$ is small at the boundaries and $\phi$ is zero at the surface. However, the $\omega \alpha$ term, shown on the left side of Fig. 10, is large during at least part of the wave evolution (see left side of Fig. 10). This term, commonly interpreted as the conversion from eddy potential to eddy kinetic energy, is discussed later in greater detail.

The importance of the divergence of the geopotential fluxes in (3.16) is further illustrated in the right-hand side of Fig. 10, which shows the contours of the sum of $+\mathbf{v} \cdot \nabla \phi$ and $(-\omega \alpha)$, together with the vectors of ageostrophic geopotential flux for 00Z/5 and 00Z/6. During the initial development, the fluxes are small and convergent in the upstream side of the energy center and divergent on the downstream side. In the decay stage, the divergence on the downstream side is predominant. Note that the energy from this center is being radiated downstream by the ageostrophic fluxes to a region where secondary development is taking place (energy center G in Fig. 5). This process is in contrast to the baroclinic evolution of normal modes (Simmons and Hoskins 1978), which have been shown to decay primarily through transfer of energy to the mean flow via Reynolds stresses. While ageostrophic geopotential fluxes can be just as large in the case of individual normal modes, the fluxes into and out of the wave are in precise balance.

The importance of the ageostrophic fluxes in the energy budget has not been adequately addressed to date, although Kung (1977) has suggested that this term may play an important role. This deficiency is due pri-
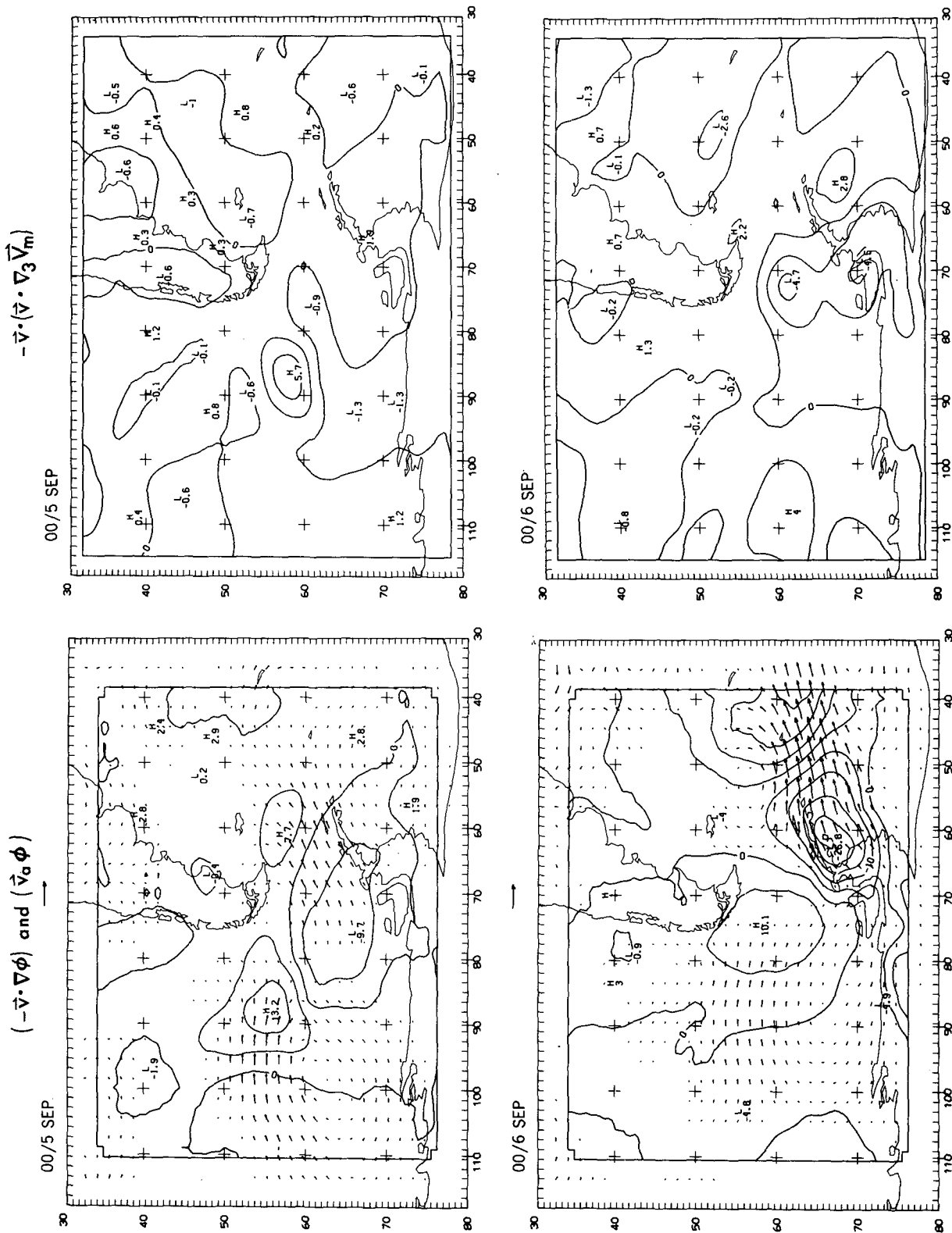
FIG. 8. Vertically averaged eddy advection of geopotential height and ageostrophic geopotential eddy flux vectors (left panels) and conversion of eddy kinetic energy by Reynolds stress (right panels). Units the same as in Fig. 7. Flux vector magnitudes as in Fig. 5.
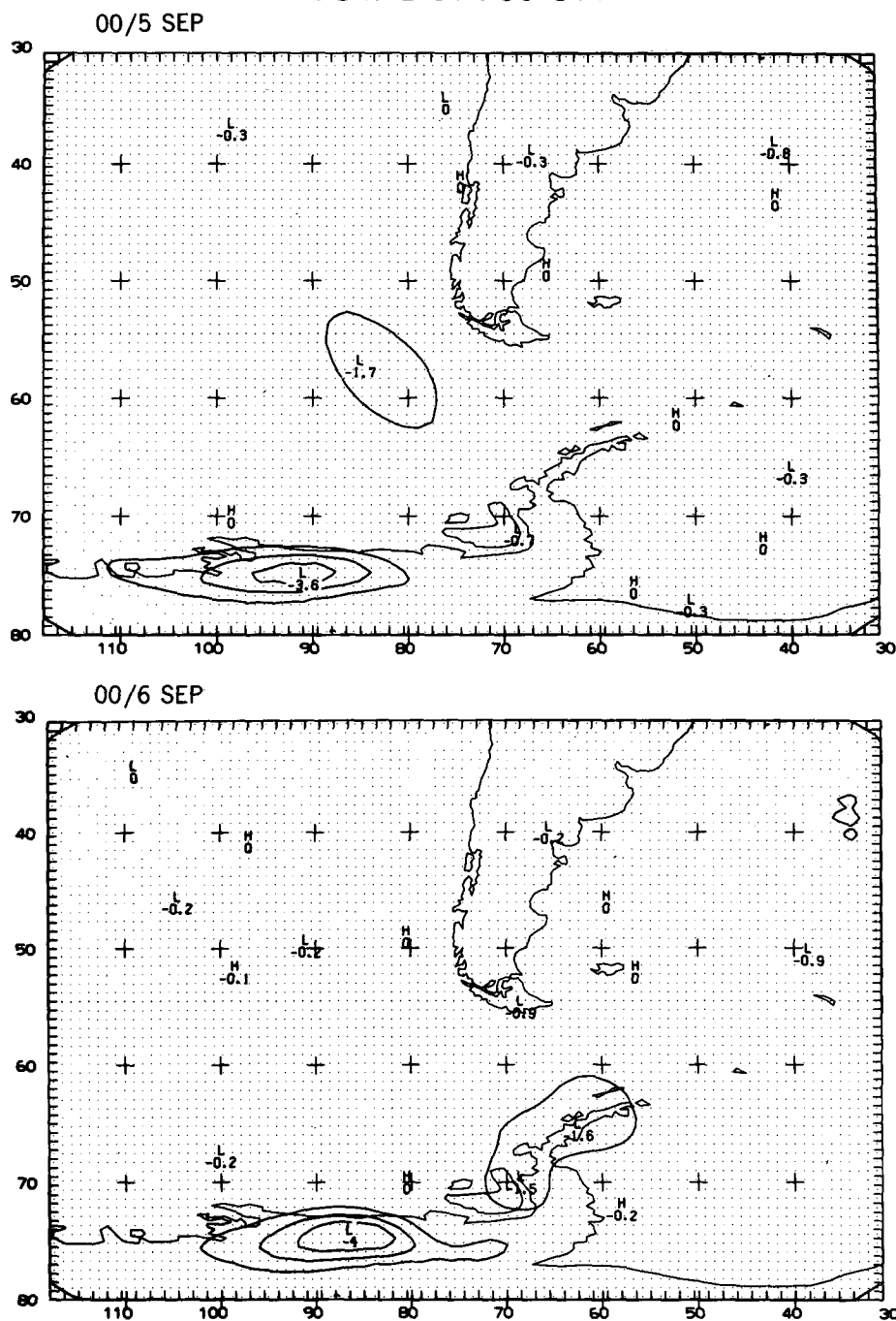
## TOTAL DIFFUSION



FIG. 9. Vertically averaged total diffusion calculated from the simulation.
Units and times are the same as in Fig. 7.

marily to the difficulty of analyzing the ageostrophic wind. In early studies, only analysis of the geostrophic wind was possible. Early global analyses issued by the meteorological centers did not provide an accurate description of the ageostrophic terms because of the strong geostrophic constraints used for the final analysis.

In terms of the wave structure, the vertically averaged $v_a \phi$ is large at the base of the trough and the ridge. In fact, although the ageostrophic *fluxes* are mainly easterly, the ageostrophic *flow* in the baroclinic wave is not, since the time deviation of the geopotential height is negative in the trough and positive in the ridge.
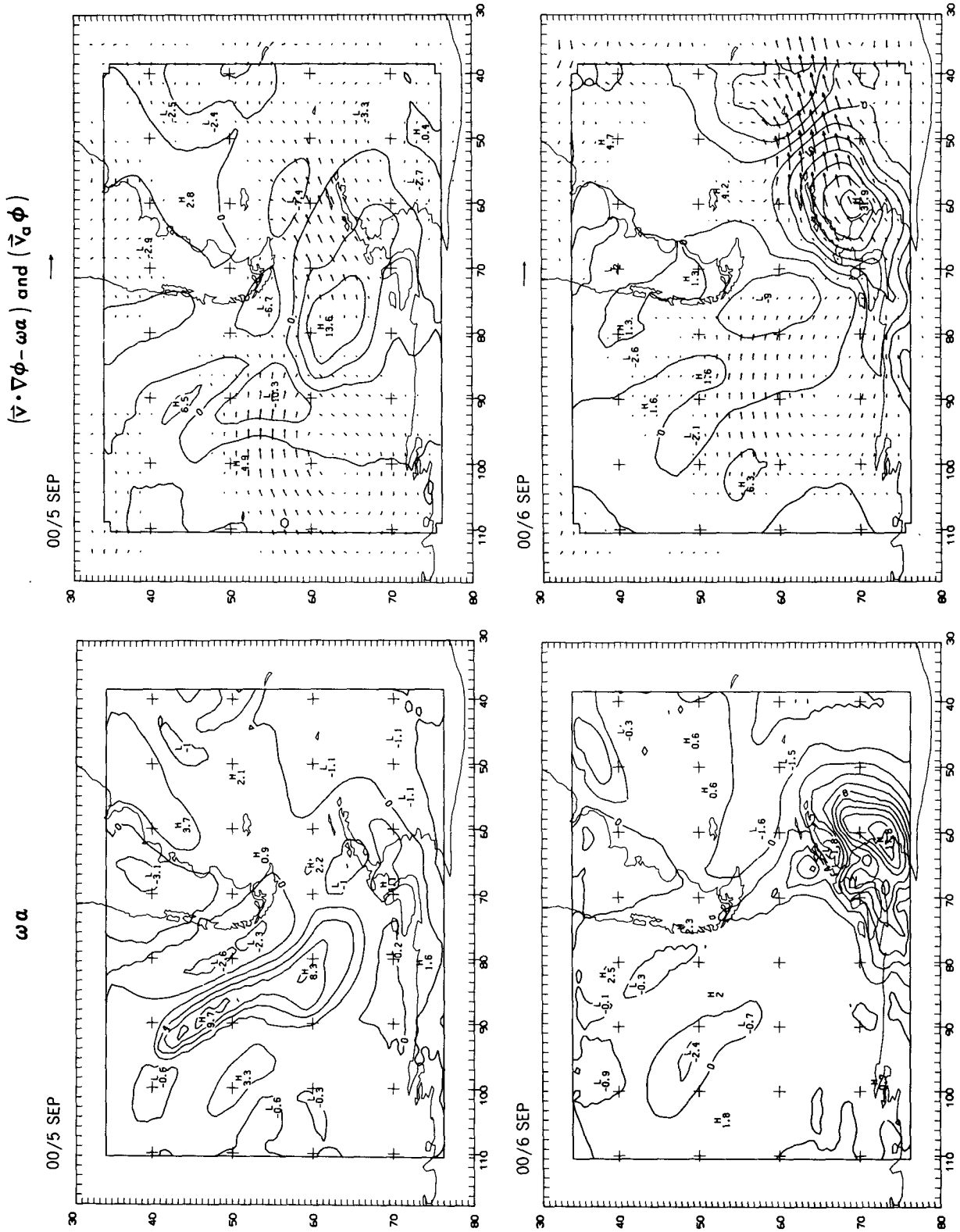
FIG. 10. Vertically averaged $\omega\alpha$ (left panels) and the sum of $+v \cdot \nabla\phi$ and $(-\omega\alpha)$, together with the ageostrophic flux vectors (right panels). Units and times are as in Fig. 7.

Therefore, the ageostrophic flow must be westward over the base of the trough and eastward over the base of the ridge. The arrows plotted in Fig. 11 indicate the total ageostrophic flow for the two time periods of interest and for both the 850- and 300-mb levels and are derived from the total wind of the numerical simulation. This flow should be very similar to the deviation from the time-mean ageostrophic flow since the time mean flow is nearly geostrophic. Figure 11 also shows the geopotential heights, and the shaded areas indicate strong negative values of omega (upward motion).

The ageostrophic flow at 850 mb in Fig. 11 is perpendicular to the axis of the ascending branch on the eastern side of the trough. As shown by Sawyer (1956), Eliassen (1962), and Orlanski and Ross (1977), the vertical shear of the geostrophic flow perpendicular to the front is the primary forcing for the ageostrophic cross-stream circulation. Therefore, the front and associated surface convergence should be at an angle to the flow, a configuration that will provide cross-stream advection of geopotential heights $-\mathbf{v} \cdot \nabla \phi$. As the wave occludes, the front and ascending branch become more parallel to the geopotential heights, reducing both the cross-stream ageostrophic flow and the kinetic energy generation (positive $-\mathbf{v} \cdot \nabla \phi$), resulting in the decay of the system. This will be discussed further in the following section.

The ageostrophic flow at 300 mb implies subgeostrophic flow in the trough and supergeostrophic flow in the ridge as seen in the right panels of Fig. 11. This configuration is responsible for the near balance between the inertial terms and geostrophic terms in the momentum equation (gradient balance).[1] Since the flow at 300 mb moves faster than the system as a whole, the baroclinic wave has a steering level at around 400 mb or 500 mb. While the gradient balance arguments for the meridional momentum equation of a slowly moving wave are reasonably satisfied, we can nevertheless complement the discussion with a vorticity argument by noting that the upper-level ageostrophic flow is westward in the cyclonic portion of the wave and eastward in the anticyclonic portion. Taking the curl of (3.1) and making the beta-plane approximation one obtains

$$\frac{d\zeta}{dt} + v\beta + \omega \frac{\partial \zeta}{\partial p} = -(f + \zeta)\nabla \cdot \mathbf{v}_a + (\nabla \times \mathbf{F}) \cdot \mathbf{k}.$$

$$(3.17)$$

In the limit of small-amplitude planetary quasi-geostrophic waves, the horizontal advection by the mean

flow, the beta effect, and the stretching term are the important contributors to the eastward or eastward wave propagation. For the cyclonic/anticyclonic centers of a planetary wave in the presence of a mean westerly flow, the propagation of the wave will be toward the west by the beta effect and toward the east due to the effects of the mean advection. The intensity of both terms depends on the horizontal scale of the systems; as the scale becomes smaller, the eastward movement due to the mean flow becomes greater. For rather short cyclone waves, the beta effect becomes rather small compared to the horizontal advection. However, since the cyclone/anticyclone centers propagate with a nearly constant velocity within a vertical column (say $\bar{U}$), which is smaller than the upper-level wind, the stretching term will oppose the horizontal advection term, i.e.,

$$(\mathbf{v} - \bar{U}) \cdot \nabla \zeta \approx -(f + \zeta)\nabla \cdot \mathbf{v}_a. \qquad (3.18)$$

The divergence of the ageostrophic flow in the upper levels over the cyclonic/anticyclonic centers will be comparable to the horizontal advection of vorticity, reducing the eastward propagation aloft.

For eastward advection in the Southern Hemisphere, $(\mathbf{v} - \bar{U}) \cdot \nabla \zeta$ is positive (negative) downstream of the cyclonic (anticyclonic) centers and negative (positive) upstream. Let us first assume that the relative vorticity is small compared with $f$. Since $f < 0$ in the Southern Hemisphere, the ageostrophic flow determined from (3.17) will be convergent on the upstream side of the cyclone center and divergent on the downstream side. For the anticyclonic center, the situation would be reversed, with divergence on the upstream side and convergence on the downstream side. This distribution can be clearly seen in the 300-mb circulation (upper right panel of Fig. 11). The ageostrophic flow is westward in the base of the trough and eastward along the ridge axis with convergence/divergence on either side. Note that as the system develops and the relative vorticity becomes large and comparable with $f$ in magnitude, the cyclonic and anticyclonic centers will experience different effects due to the divergence of the ageostrophic flow. Note also from (3.17) that, since $(f + \zeta)$ is more negative over the cyclonic center than over the anticyclonic side, and if the eastward horizontal advection is approximately the same for both centers, the effect of the nonlinearity due to the relative vorticity is to produce a stronger westward acceleration on the cyclonic center than on the anticyclonic center. The net result is that the anticyclonic center will tend to move eastward faster and deform the wave, as seen in the lower right panel of Fig. 11. This particular system has a relatively strong ridge development, with the intensity of the relative vorticity in the anticyclonic comparable to that of the cyclone. For other cases in which the cyclonic vorticity is significantly larger than the anticyclonic vorticity, the wave structure may differ from that shown in Fig. 11. The relationship between

---

[1] James Holton, through independent work involving statistical analyses of a North Pacific storm track (described in a seminar given at GFDL on 7 June 1990), found that baroclinic waves had an ageostrophic circulation that resembled this case, and his explanation for the upper-level structure of the ageostrophic flow was similar to that presented here.
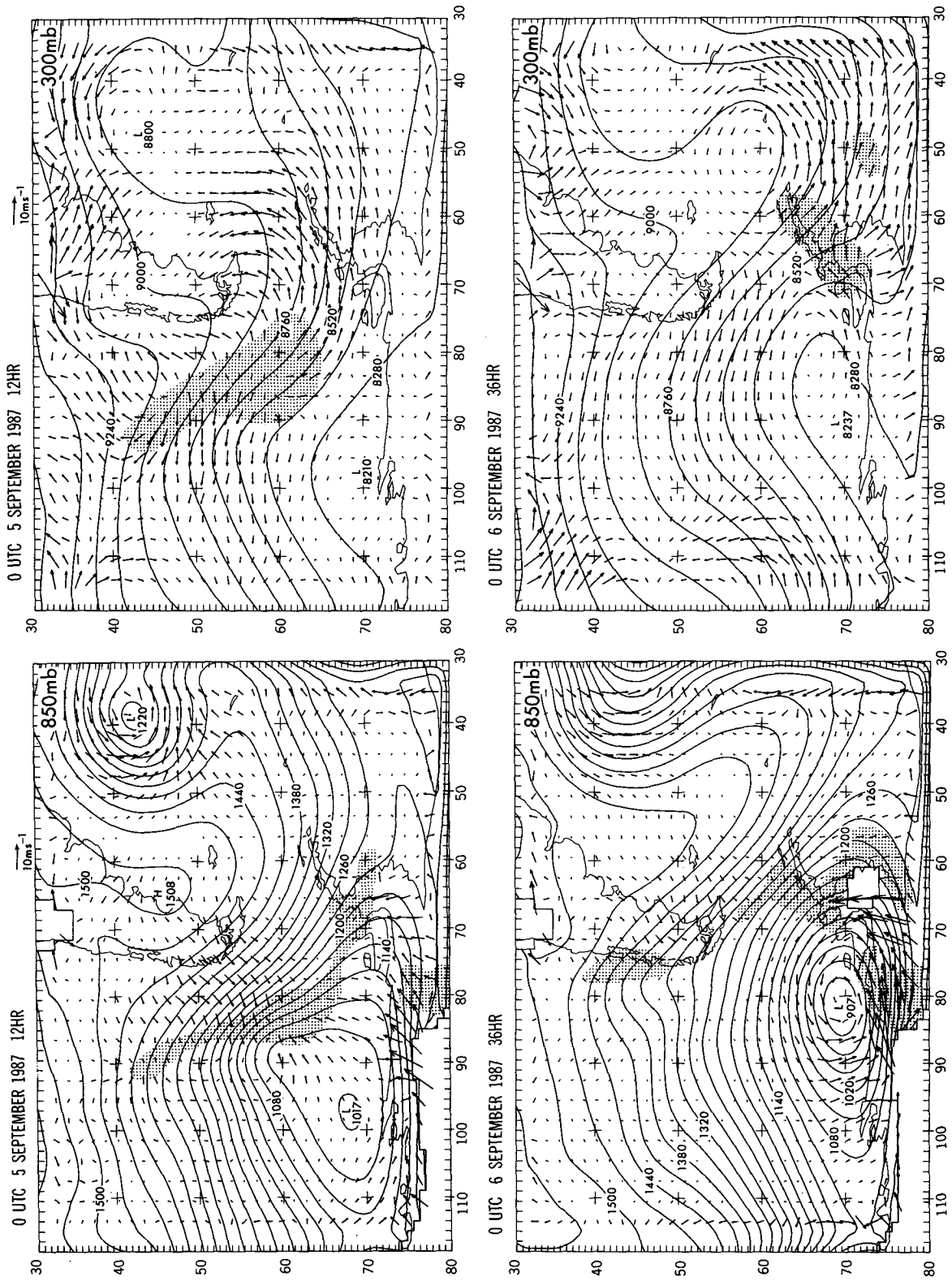
GEOPOTENTIAL HEIGHT and AGEOSTROPHIC FLOW

FIG. 11. Geopotential height (solid), ageostrophic flow (vectors), and ω (shaded) from the simulation at 850 mb (left panels) and 300 mb (right panels), for 0000 UTC 5 September (upper graphs) and 0000 UTC 6 September (lower graphs).

the ageostrophic flow and the local dynamics of the occluded system has also been analyzed and will be published separately.

### f. Volume budget of the $K_e$ equation

It is clear from the previous discussion that the disparity in the magnitude of some terms in (3.14), together with the large positive and negative values associated with the advection of $K_e$, makes it difficult to evaluate the net relative contributions to the local tendency directly. A volume integral of each term of (3.14) would permit better interpretation of the net contribution of that term. However, it is difficult to isolate the area of interest for proper evaluation in the case of a specific moving disturbance. If $K_e$ was a conservative quantity, then one could isolate a volume bounded by a contour of constant $K_e$, in which case such a boundary would constitute a material surface and the fluxes of $K_e$ through that surface would be identically zero. Unfortunately, this is not the case. However, an integral of the fluxes over a constant $K_e$ boundary of a volume that captures the bulk of the $K_e$ associated with the disturbance in question and is sufficiently isolated from other packets of $K_e$ should yield boundary fluxes that, although not necessarily zero, would be of a magnitude more readily comparable to the contributions from other terms. Following this approach, a volume boundary was chosen as the $K_e = 300 \ m^2 \ s^{-2}$ contour (see the enhanced contour on the left of Fig. 6) and the evolution of $K_e$ inside this domain was analyzed.

The volume integrals of the kinetic energy components are shown as a function of time in the top panel of Fig. 12. Within the chosen volume, the eddy component dominates the total, reaching a maximum at 00Z/6 (36 h into the simulation). The $K_m$ component is roughly one-third of the total, and the $K_1$ component is slightly negative, indicating the perturbation flow is, on balance, in a direction opposite to the mean flow.

The important contributions to the evolution of $K_e$, as described by (3.14) are shown in the middle panel of Fig. 12. The volume integral of the local tendency $\partial K_e/\partial t$ is dashed, $-\mathbf{v} \cdot \nabla \phi$ is solid, $-\mathbf{V}_m \cdot \nabla K_e$ is dotted, and the contribution of the conversion by Reynolds stresses $-\mathbf{v} \cdot (\mathbf{v} \cdot \nabla_3 \mathbf{V}_m)$ is dot-dashed. First, note that during the early part of the growth (i.e., positive $\partial K_e/\partial t$), the Reynolds stress term is positive, indicating a small positive barotropic contribution to the growth of eddy kinetic energy. This contribution turns negative about halfway through the growth stage, indicating a drain of eddy kinetic energy, presumably to the mean flow, as in the idealized baroclinic instability studies (Simmons and Hoskins 1978). However, the eddy kinetic energy advection and $-\mathbf{v} \cdot \nabla \phi$ terms dominate, yielding a net positive local tendency. In the later part of the evolution, the kinetic energy tendency turns negative due to a sharp reversal in the sign of $-\mathbf{v} \cdot \nabla \phi$. This result is significantly different from the results of

Simmons and Hoskins (1978) for nonlinear baroclinic waves within zonal flows. The fact is that in the case of waves evolving within zonal flows, the volume integral of the term $-\mathbf{v} \cdot \nabla \phi$ is equal to minus the integral of $\omega \alpha$, which for baroclinic evolutions is positive and the sole source of $K_e$. In this case, however, the divergence of the geopotential fluxes that developed in the later stage of the wave evolution dominated the positive contributions from $\omega \alpha$. These terms are displayed in the lower panel of Fig. 12, where $\partial K_e/\partial t$ is shown as solid line, $\omega \alpha$ is indicated as a dot-dash line, and the volume integral of the divergence of the geopotential fluxes is the dashed line. These results corroborate the conclusions derived with regard to Fig. 8. Thus, eddy kinetic energy $K_e$ decays primarily because large geopotential fluxes remove energy locally, exporting it downstream where secondary development may occur.

It is clear from the previous discussion that geopotential flux can explain the cessation of growth in the upper-level amplitudes. The downstream development observed in this case is similar to that described by Simmons and Hoskins (1979), with perhaps the main difference being that, in their case of waves reaching a finite amplitude in zonal flows, the source of $K_e$ (primarily $\omega \alpha$) is balanced by the upper-level fluxes that export energy upstream and downstream from the wave energy center. At this stage the wave packet undergoes translation without amplitude changes. In our case, however, the mean flow is not zonal and the developing wave experiences constantly changing conditions as it propagates eastward, eventually decaying via strong downstream fluxes. Eddy energy is then radiated to a new system developing farther downstream. The energy cycle for these waves seems to be characterized by baroclinic generation, strong advection, and ultimately decay by the radiation of energy. In the next section, we will present additional results confirming the conclusions reached regarding $K_e$ evolution and extend what we have learned to total eddy energy.

## 4. Total eddy energy evolution

In the last ten years, the theory of eddy–mean flow interaction has been greatly expanded (i.e., McIntyre 1980; Andrews and McIntyre 1976; Edmon et al. 1980; Plumb 1983, 1985). Some of these studies have questioned the classical interpretation of the energy cycle (Lorenz 1955). In particular, it has been pointed out that the individual conversion terms and flux vectors are not good indicators of wave propagation or generation characteristics (McIntyre 1980; Plumb 1983). Plumb (1983) reviewed the traditional derivation of the energy cycle and noted the paradoxical properties of the energy conversion and flux terms for steady, conservative motion. There is a certain lack of conciseness in the classical as well as in a new proposed transformed Eulerian mean (TEM) energy budget for the individual conversion and flux terms. A nonzero
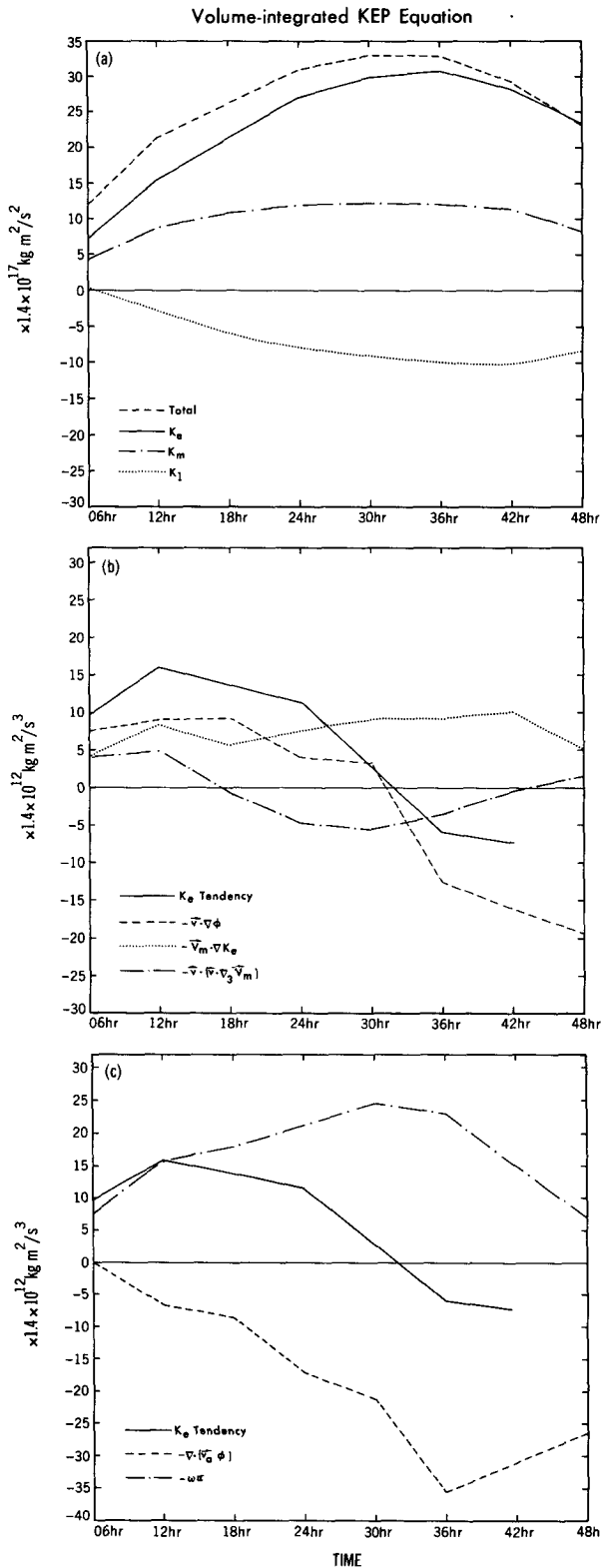
## Volume-integrated KEP Equation



FIG. 12. Volume integral (bounded by the 300 m² s⁻² eddy kinetic energy contour, see text) of total kinetic energy (dashed), $K_m$ (dot-dashed), $K_1$ (dot), and $K_e$ (solid) in the upper graph. In the middle panel, the local energy tendency of eddy kinetic energy (solid), the

divergence of the traditional time-mean energy flux vector, $\overline{\mathbf{v}\Phi}$, does not necessarily indicate an increase of wave activity. An interdependence of the flux divergence and the conversion between the eddy and the time-mean flows was noted by Dickinson (1969) and Hartmann (1976) and was demonstrated by Plumb (1983). Plumb also derived a new energy cycle using the transformed Eulerian mean equations that eliminated the $P_z$ to $P_e$ conversion terms (where $P$ is the potential energy, $K$ is the kinetic energy, $z$ is a zonal mean, and $e$ is the eddy component). In fact, the energy flow for baroclinic waves was from $P_z$ to $K_z$ to $K_e$ and finally to $P_e$. This apparently surprising result can just as easily be interpreted in the context of the classical energy cycle where, by adding a constant to all the conversion terms, one can change the direction of the energy conversion in the traditional four box diagram (Orlanski 1968). Take, for example, $CP_zP_e$, the conversion from zonal potential energy, $P_z$, to eddy potential energy, $P_e$. Subtracting this term from the four conversion terms, $CP_zP_e$, $CP_zK_z$, $CK_zK_e$, and $CK_eP_e$ (using the same notation convention as for $CP_zP_e$), results in an energy flow similar to the TEM approach proposed by Plumb. The conversion between $P_z$ and $P_e$ is zero and the energy cycle will be from $P_z$ to $K_z$ to $K_e$ to $P_e$. Plumb's main point was that all energy budgets have some ambiguities if partial terms are analyzed. Only the total contributions of the fluxes and conversions have a unique meaning.

In this section, we consider the evolution of the total eddy energy distribution for the 3–6 September 1987 period. The equation for eddy available potential energy is derived in a manner analogous to that of eddy kinetic energy above, and the relationship between the horizontal heat fluxes, which are a major source of eddy potential energy, and the ageostrophic geopotential fluxes is discussed. Last, total eddy energy and the ageostrophic geopotential flux are used to derive the relative group velocity of the energy packet comprising the specific storm under study.

### a. Eddy available potential energy density equation

In a fashion similar to the derivation of the eddy kinetic energy (3.14), we can proceed to define an eddy available potential per unit mass as

$$AP_e = -\left( \frac{\alpha_m}{2\Theta_m} \frac{1}{d\tilde{\Theta}/dp} \theta^2 \right). \tag{4.1}$$

This definition is similar to that used by Plumb (1983), except that the vertical coordinate is pressure instead of log pressure. In (4.1), $\alpha$ is the inverse of the density,

horizontal advection of $K_e$ by the mean wind (dotted), $-\mathbf{v} \cdot \nabla \phi$ (dashed), and the conversion by Reynolds stresses (dot-dash) are shown. Lower panel shows the local tendency of $K_e$ (solid), $-\omega\alpha$ (dot-dash), and the divergence of the ageostrophic fluxes (see text).

$\Theta$ is the potential temperature as defined in (3.6), and $\theta$ is the deviation of $\Theta$ from its time mean. The ($\hat{}$) indicates the horizontal area average, and, as before, the $m$ subscript indicates the time mean. The horizontal and areal average of $d\Theta/dp$ represents the reference state required by the definition of the available energy (Lorenz 1955).

Multiplying the time deviation of (3.6) by

$$-\frac{\alpha_m}{\Theta_m}\frac{\theta}{d\tilde{\Theta}/dp}$$

and rearranging the terms we get

$$\frac{\partial}{\partial t}AP_e + \mathbf{V}_m \cdot \nabla_p AP_e + \mathbf{v} \cdot \nabla_3 AP_e$$

$$= \omega\alpha + \frac{\alpha_m}{\Theta_m}\frac{\overline{v\theta}}{d\tilde{\Theta}/dp} \cdot \nabla_p\Theta_m$$

$$- \theta\left(\frac{\alpha_m}{\Theta_m}\frac{\overline{\mathbf{v}}}{d\tilde{\Theta}/dp} \cdot \nabla_p\theta\right) + S. \quad (4.2)$$

Again, an overbar is used to indicate the time mean of the product. The terms in the $AP_e$ equations have meanings similar to those in (3.14). The first term on the rhs is usually interpreted as the conversion from $AP_e$ to $K_e$, while the second term on the rhs is the conversion from the time-mean available potential energy to $AP_e$. The third term on the rhs is the correlation between the perturbation temperature and its time-mean advection by the eddies. The time mean of this term is zero, but even its instantaneous values are small. The last term on the left side represents advection of $AP_e$ by the eddies, which is usually neglected in time-average budget but is retained here. The quantity $S$ represents the nonconservative sources and sinks of eddy potential energy.

Of course, one of the most important terms contributing to $S$ is the diabatic effect of latent heat release. The model simulation described in OKMM included moist convective parameterization, and, while it was not possible to isolate the eddy component of this energy release, the total latent energy release was explicitly calculated, although it is not shown here. This particular storm was accompanied by deep convection along a narrow band on the eastern side of the trough, but the associated latent energy release resulted in only a small contribution to the total energy budget.

The total eddy energy density is defined as

$$TE_e = \frac{1}{2}\mathbf{v} \cdot \mathbf{v} - \left(\frac{\alpha_m}{2\Theta_m}\frac{1}{d\tilde{\Theta}/dp}\theta^2\right). \quad (4.3)$$

The time evolution of the vertically averaged $TE_e$, shown in Fig. 13, is similar to the $K_e$ evolution shown in Fig. 5, and all of the $K_e$ centers discussed previously can also be identified in the distribution of $TE_e$. The geopotential fluxes due to the ageostrophic flow also

are shown and clearly depict convergence (gain) upstream of energy center D (see Fig. 5) and divergence (loss) downstream. In particular, as the energy packet decays, large divergences of $v_a\phi$ are evident. At the same point in time, the downstream convergence of these fluxes corresponds to an area where energy is increasing. The time evolution of $TE_e$ and its components, integrated over the volume within the 300 m$^2$ s$^2$ $TE_e$ contour, is shown in Fig. 14. Here $TE_e$ attains a maximum at around the same time as $K_e$. Note that $AP_e$ is always smaller than $K_e$, which could be interpreted as characteristic of this cyclone system, which has a length scale smaller than the Rossby radius of deformation.

### b. Eddy heat and geopotential fluxes

Individual terms in the $AP_e$ budget will not be discussed in detail as was done with regard to the eddy kinetic energy budget (3.14), since the mean and eddy advection described by (4.2) are analogous to those discussed with respect to $K_e$ and were shown in Fig. 7, and because the $\omega\alpha$ term is constant to both the $K_e$ and $AP_e$ equations; its distribution was shown earlier in Fig. 10. The $\omega\alpha$ term represents a sink of $AP_e$ and a source of $K_e$, as predicted by the theories of baroclinic evolution. This sink of $AP_e$ is, however, secondary to the strong source of $AP_e$ provided by the poleward transport of heat by the eddies, $\overline{v\theta}$. We shall therefore focus our discussion of (4.2) on the eddy heat flux terms.

Since $\nabla\Theta$ is positive in the extratropics of the Southern Hemisphere and $d\tilde{\Theta}/dp$ is negative, a negative heat flux will result in an increase of $AP_e$, as shown on the left of Fig. 15. Note that the horizontal heat fluxes are largely in phase with $\omega\alpha$ throughout the evolution of the system, with regions of $AP_e$ generation by the heat fluxes corresponding quite closely to the regions of conversion of $AP_e$ to $K_e$ by $\omega\alpha$. Note also that as the energy packet grows, so too does the horizontal heat flux, similar to the zonally averaged budgets found by Simmons and Hoskins (1979). They also found that while the conversion from $CP_zP_e$ reached its maximum at the time of maximum eddy energy, the removal of energy by the Reynolds stresses $CK_zK_e$ also was large and in the end dominated the energy growth. In our study, however, ageostrophic geopotential fluxes dominated the energy tendency during the decay stage of the cyclone.

Determining the relationship between heat fluxes and ageostrophic geopotential fluxes is crucial, since the growth of one implies growth of the other. This relationship can, at least in general terms, help to explain why a finite-amplitude wave reaches equilibrium without necessarily altering the local mean flow conditions. It is an observational fact that the intensification of a wave ceases when the system becomes occluded (i.e., no vertical tilt). At this stage, $\mathbf{V} \cdot \nabla\Theta$ is

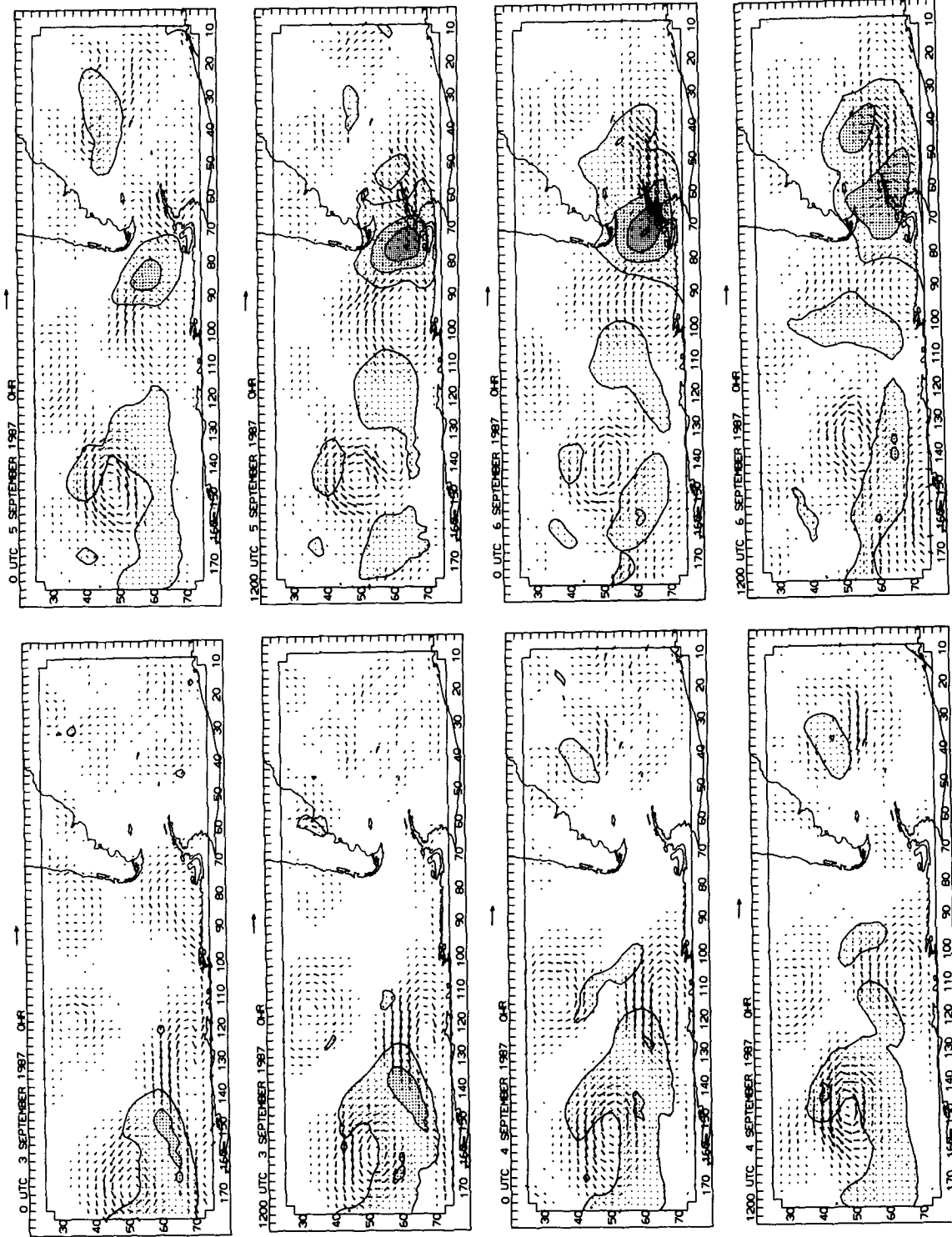## TOTAL EDDY ENERGY AND AGEOSTROPHIC GEOPOTENTIAL FLUX

FIG. 13. Vertically averaged eddy total (kinetic plus available potential) energy and ageostrophic geopotential height flux vectors at 12 h intervals, from 0000 UTC 3 September to 1200 UTC 6 September. Light, medium, and dark shading correspond to 250–500 m² s⁻², 500–750 m² s⁻², and greater than 750 m² s⁻², respectively. Vectors units are the same as in Fig. 5.
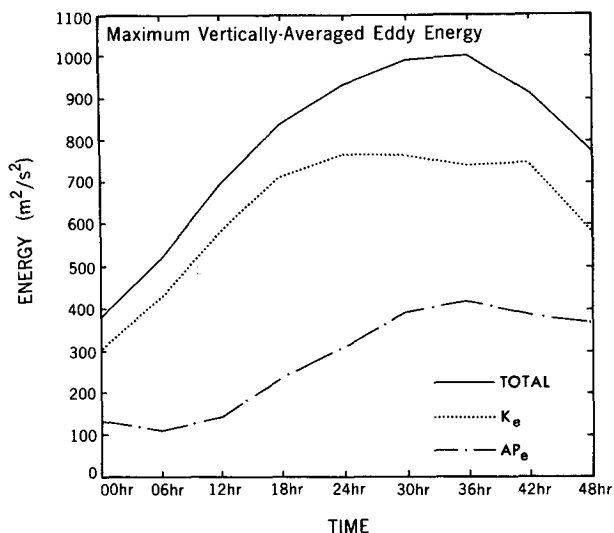
FIG. 14. Maximum vertically averaged total energy (solid), $K_e$ (dotted), and eddy available potential energy (dot-dash) as a function of time.

nearly zero at low levels, implying very little total advection of heat. Assuming the flow is quasi-geostrophic, $\mathbf{V} \cdot \nabla \Theta$ implies that the contours of $\Phi$ and $\Theta$ are locally parallel and therefore $\Theta = F(\Phi)$. This relationship can been seen in any fully developed wave as the contours of potential temperature and geopotential at the lower levels become quite parallel along the eastern side of the trough (Orlanski et al. 1990). Following this reasoning, the time deviation of potential temperature can be expressed as a function of the time deviation of geopotential height, $\theta = F_\Phi(\Phi)\phi$, so that

$$v\theta = F_\Phi v\phi. \tag{4.4}$$

Equation (4.4) states that in an occluded wave the horizontal heat fluxes are proportional to the horizontal geopotential fluxes. The eddy geopotential fluxes for the September 1987 storm are displayed on the right of Fig. 15. Note that during the early development of the wave, there is no correspondence between the geopotential flux and the heat fluxes. Only at the mature stage of the cyclone are the regions of poleward flux similar.

Thus, equilibration of the wave occurs as the wave occludes, despite the continued conversion of $AP_m$ to $AP_e$, due to the fact that geopotential fluxes become large, exporting the wave energy to a neighboring system. What remains to be shown is that as the total geopotential eddy fluxes grow, the ageostrophic fluxes also grow, since it is the divergence of those fluxes that removes the energy. Although we assume that this relation exists, this has not been proven.

## c. Relative group velocity

A phase average (to eliminate wave-phase dependence) of the geopotential fluxes for an energy-con-

servative, quasi-geostrophic, small-amplitude wave train will be proportional to the product of the eddy energy and the group velocity relative to the mean flow (i.e., Pedlosky 1979, p. 351). Although the time evolution of the eddy field in this case cannot be regarded as small compared with the steady mean flow (see Fig. 7) and the eddy energy is not strictly conserved, application of such a theoretical framework to this case study can provide a means of determining the propagation characteristics associated with the wave activity.

Assuming that a volume integral of the ageostrophic fluxes is independent of the wave phase, the relative group velocity, $\mathbf{C}_{gr}$, can be defined as

$$\mathbf{C}_{gr} = \mathbf{C}_g - \mathbf{V}_m \approx \frac{\int\int_{p_t}^{p_s} \mathbf{v}_a \phi \, dp \, dA}{\int\int_{p_t}^{p_s} TE_e \, dp \, dA}. \tag{4.5}$$

The relative group velocity, calculated from the simulation every 6 h, is shown by the vectors plotted in Fig. 16, together with the 300 m$^2$ s$^{-2}$ total energy contour used for the volume integral. The vector origins are located at the energy maxima of the corresponding time period. Note that the energy packet boundary expands with time as it undergoes a poleward translation. As was shown earlier (see Fig. 7), this poleward translation is due primarily to the eddy advection. At the early, growing stages the relative group velocity is small and in fact remains small compared to the mean flow for the entire period. However, at later times (30–48 h into the stimulation), the relative group velocity becomes larger and develops an equatorward component, pointing toward a new trough developing downstream. It should be noted that this new trough downstream of the decaying center is actually located on the eastern side of a ridge separating the maxima of $K_e$. In addition, the ridge itself intensifies markedly during the period. The ageostrophic geopotential fluxes and the relative group velocity point northeast through this ridge. Note that a time integral of the group velocity distribution taken over the evolution of an ensemble of cyclones would show a predominantly eastward component in the region where the main development took place and a more equatorward component in the region where the storm dissipated. Although these results are in complete agreement with the analysis of the $E$-vector distribution along a storm track made by Hoskins et al. (1983), the distribution of the group velocity or (when equivalent) the $E$-vectors may not give a specific indication of which processes dominate the decay of wave energy. Hoskins et al. showed that the $E$-vector distribution was a result of wave–mean flow interaction, whereas it has been found in the present case that the group velocity distribution was consistent with wave energy loss to other systems and not necessarily to the mean flow. A complete discussion on the analysis of
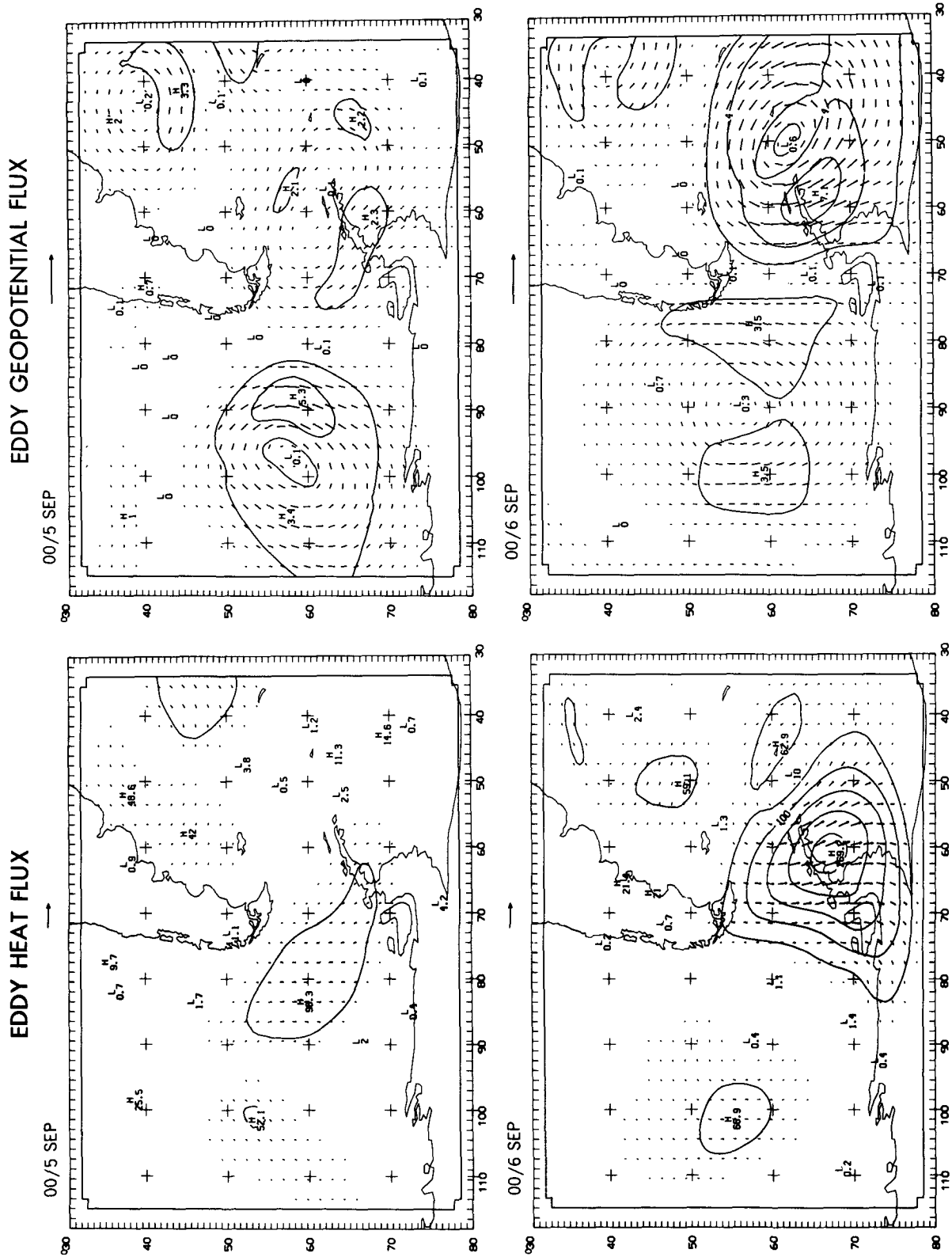
EDDY GEOPOTENTIAL FLUX

EDDY HEAT FLUX

FIG. 15. Vertically averaged eddy heat fluxes (left panels, contour interval: 50 m s⁻¹ K, vector length indicates 50 m s⁻¹ K) and eddy geopotential fluxes (right panels, contour interval: $2 \times 10^4$ m³ s⁻³, vector length indicates $2 \times 10^5$ m³ s⁻³). Times are the same as in Fig. 7.
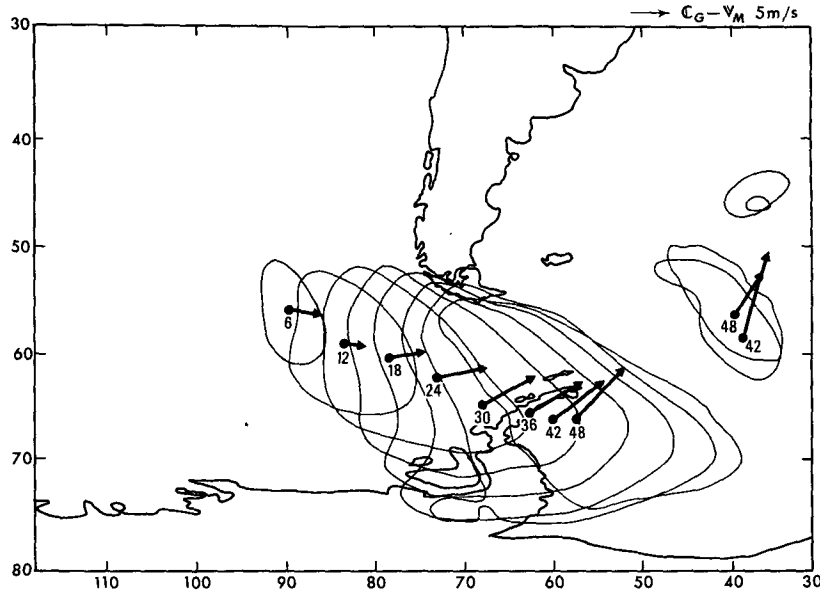
FIG. 16. Relative group velocity vector calculated every 6 h from the simulation, and the 300 m² s⁻² total eddy energy contour used for the volume integral (see text).

quasi-geostrophic wave activity for this case will be published elsewhere.

## 5. Summary and conclusions

. The evolution of cyclones in the Southern Hemisphere has been investigated using ECMWF data for September 1987, and a high-resolution model simulation has been employed to evaluate the energy budget of a specific storm during this period. It is apparent from the data that cyclone waves in the Southern Hemisphere may develop quite differently from those in the Northern Hemisphere. One difference on the planetary scale is the dual-jet structure, which is evident in the sector zonal mean for at least part of the middle and high latitudes of the Southern Hemisphere and which is conducive to the development of unstable barotropic and baroclinic eddies (Trenberth 1986b). In early September, the intensification of an anticyclone in the region between the two jets resulted in a merging of the subtropical and polar westerlies on the eastern side of the downstream wave trough. This merger led to the advection of warm, moist subtropical air to subpolar latitudes, as shown by the PV anomalies on the 320 isentropic surface, setting the stage for baroclinic enhancement of the wave. The subsequent secondary development was much more intense.

The eddy energy budget has been applied to the region where this strong development occurred. The time evolution of the eddy kinetic energy center (or "packets") has been used to illustrate the complete evolutionary cycle of the storm, from incipient disturbance through its growth, maturation, and eventual decay.

The energy center displayed an eastward propagation velocity, which was slightly faster than the 30-day time-mean wind speed. A detailed eddy kinetic energy budget revealed that $-\mathbf{v}_a \cdot \nabla\phi$ comprised the *major source* of eddy kinetic energy during the development stage of the cyclone, consistent with the characteristics of baroclinic development. What was more surprising was that this term also comprised the *major sink* of energy during the decay stage. While transfer of energy by Reynolds stresses $-\mathbf{v} \cdot (\mathbf{v} \cdot \nabla_3 \mathbf{V}_m)$ was also found to be a sink of eddy kinetic energy, its magnitude was too small to explain the decay of the system. This finding marks the primary difference between this case of localized evolution and the results of studies of the life cycle of normal-mode type baroclinic waves in zonal flows, which have been shown to decay primarily by transfer of energy to the mean flow by Reynolds stresses. This difference can be explained by the fact that, while ageostrophic fluxes can be just as large in the case of the individual normal modes, the fluxes into and out of the wave are precisely balanced. The positive values of $-\mathbf{v}_a \cdot \nabla\phi$ in the developing stage of the wave were found to be due to the dominance of the $\omega\alpha$ component. The strong negative local tendencies of eddy kinetic energy due to $-\mathbf{v}_a \cdot \nabla\phi$ during the decay stage of the wave evolution was produced by divergence of the geopotential height fluxes, $-[\nabla \cdot (\mathbf{v}_a\phi)]$. It was found that when the wave attained a sufficiently large amplitude, it became "occluded," and the horizontal heat flux, mainly poleward, reached its maximum amplitude. However, the ageostrophic fluxes also became very large at this stage and, on the downstream side of the eddy kinetic energy center, were

strongly divergent. Farther downstream, these fluxes became convergent, triggering the development of a new energy center. Energy removal by internal dissipation was found to be small, and dissipation of kinetic energy by friction was calculated to be only about one-third of the changes in kinetic energy due to $-\mathbf{v}_a \cdot \nabla \phi$. The relatively small value of dissipation is likely due to the fact that this storm developed over open ocean.

This analysis also points out that the upper-level ageostrophic flow produced by strong divergence of the ascending branch is responsible for the work done by pressure forces. Upstream of the jet maximum the ageostrophic flow is westward toward lower pressure and into the trough base. In the exit region, the ageostrophic flow is eastward toward higher pressure and the ridge axis, resulting in supergeostrophic winds in the ridge and subgeostrophic winds in the trough. An integral of all of the terms in the eddy kinetic energy equation, carried out over a volume bounded by a contour of eddy kinetic energy, clearly indicates the dominant role of $\omega\alpha$ during the developing stage and of $-[\nabla \cdot (\mathbf{v}_a \phi)]$ during the decay stage. It should also be noted that while most of the $K_e$ centers (shown in Figs. 5 and 13) were associated with convergence of ageostrophic geopotential fluxes from other centers upstream, in none of the cases was energy found to propagate upstream (i.e., no upstream development).

It has been found, at least in this particular case study, that a careful analysis of the energy budget can provide valuable insight into the storm's evolution. *The wave initially grew primarily through poleward fluxes of heat, consistent with baroclinic theory. However, the system evolved only up to the point where the source of eddy energy, mainly the poleward advection of heat by the horizontal eddy heat fluxes, was compensated for by the dispersion of eddy energy, appearing mainly as an eastward ageostrophic geopotential flux.* Energy exported in this fashion can provide the initial triggering mechanism for downstream development provided that the proper baroclinic environment exists to support its subsequent evolution. It has been shown in this paper that ageostrophic fluxes should prove to be especially useful predictive tools in cases where latent heating and other diabatic effects are not very important. It remains to be seen whether they could also prove useful under more general conditions.

## APPENDIX

### The K1 Equation

An equation for the time evolution of the correlations between the time-mean velocity and the time deviation of velocity can be obtained by multiplying (3.11) by $\mathbf{v}$ and (3.12) by $\mathbf{V}_m$ and adding them together to yield

$$\frac{\partial K_1}{\partial t} + \mathbf{V}_m \cdot \nabla K_1 + \mathbf{v} \cdot \nabla K_m + \mathbf{v} \cdot \nabla K_1 - \overline{(\mathbf{v} \cdot \nabla K_1)}$$

$$= \mathbf{vv} \cdot \nabla \mathbf{V}_m - (\overline{\mathbf{vv}} \cdot \nabla \mathbf{V}_m) - (\mathbf{V} \cdot \nabla \Phi)'$$

$$- [(\mathbf{F}_o \cdot (\mathbf{V}_m - \mathbf{v})] + (\text{diss})', \quad (A.1)$$

where $(AB)' = A_m b + a B_m$ and lowercase letters refer to deviations from the time mean. Note that all the terms have zero time mean except for $F_o V_m$, the time mean of which equals the time tendency integral of $K_1$. Equation (A.1) can be decomposed into divergences of flux vectors and conversion terms from $K_e$ to $K_1$ (designated $C_{e1}$) and $K_1$ to $K_m$ (designated $C_{1m}$). The resulting energy budget can be interpreted in a manner similar to the time-mean flow. Although wave energy is contained in both $K_e$ and $K_1$, as well as the mean flow, $K_m$, it is possible to interpret the energy distribution in such a way that the eddy energy is represented solely by $K_e$, even on an instantaneous basis, and that $K_1$ contributes solely to the evolution of the mean flow, as represented by the time average of the conversion terms $C_{e1}$ and $C_{1m}$.

## REFERENCES

Andrews, D. G., and M. E. McIntyre, 1976: Planetary waves in horizontal and vertical shear: The generalized Eliassen–Palm relation and the mean zonal acceleration. *J. Atmos. Sci.,* **33,** 2031–2048.

Charney, J. G., 1947: The dynamics of long waves in a baroclinic westerly current. *J. Meteor.,* **4,** 135–162.

——, and M. E. Stern, 1962: On the stability of internal baroclinic jets in a rotating atmosphere. *J. Atmos. Sci.,* **19,** 159–172.

Cressman, G. P., 1948: On the forecasting of long waves in the upper westerlies. *J. Meteor.,* **5,** 44–57.

Dickinson, R. E., 1969: Theory of planetary wave–zonal flow interaction. *J. Atmos. Sci.,* **26,** 73–81.

Eady, E. T., 1949: Long waves and cyclone waves. *Tellus,* **1,** 33–52.

Edmon, H. J., Jr., B. J. Hoskins and M. E. McIntyre, 1980: Eliassen–Palm cross sections for the troposphere. *J. Atmos. Sci.,* **37,** 2600–2616.

Eliassen, A., 1962: On the vertical circulation in frontal zones. *Geofys. Publ.,* **24,** 147–160.

Farrell, B., 1982: The initial growth of disturbances in a baroclinic flow. *J. Atmos. Sci.,* **39,** 1663–1686.

Frederiksen, J. S., 1983: Disturbances and eddy fluxes in Northern Hemisphere flows: instability of three dimensional January and July flows. *J. Atmos. Sci.,* **40,** 836–855.

Gall, R., 1976: Structural changes of growing baroclinic waves. *J. Atmos. Sci.,* **33,** 374–390.

Gill, A. E., 1982: *Atmosphere–ocean Dynamics.* Academic Press, 662 pp.

Haltiner, G. J., and R. T. Williams, 1979: *Numerical Prediction and Dynamic Meteorology.* 2nd ed. Wiley & Sons, 477 pp.

Hartmann, D. L., 1983: Barotropic instability of the polar night jet stream. *J. Atmos. Sci.*, **40**, 817–835.

Hoskins, B. J., M. E. McIntyre and A. W. Robertson, 1985: Isentropic potential vorticity maps. *Quart. J. Roy. Meteor. Soc.*, **111**, 877–946.

Kung, C. F., 1977: Energy sources in middle-latitude synoptic-scale disturbances. *J. Atmos. Sci.*, **34**, 1352–1365.

Kuo, A. L., 1949: Dynamic instability of two-dimensional nondivergent flow in a barotropic atmosphere. *J. Meteor.*, **6**, 105–122.

Lorenz, E. N., 1955: Available potential energy and the maintenance of the general circulation. *Tellus*, **7**, 157–167.

McIntyre, M. E., 1980: An introduction to the generalized Lagrangian-mean description of wave, mean-flow interaction. *Pure Appl. Geophys.*, **118**, 152–176.

Merkine, L.-O., 1977: Convective and absolute instability of baroclinic eddies. *Geophys. Astrophys. Fluid Dyn.*, **9**, 129–157.

Miles, M. K., 1959: Factors leading to the meridional extension of thermal troughs and some forecasting criteria derived from them. *Meteor. Mag.*, **88**, 193–203.

Nakamura, N., 1988: Dynamics of baroclinic instability in rapid cyclogenesis. Ph.D. thesis, Princeton University, 104 pp.

Namias, J., and P. F. Clapp, 1944: Studies of the motion and development of long waves in the westerlies. *J. Meteor.*, **1**, 57–77.

Newell, R. E., J. W. Kidson, D. G. Vincent and G. J. Boer, 1974: *The General Circulation of the Tropical Atmosphere, and Interactions with Extratropical Latitudes. Vol. 2,* The MIT Press, 371 pp.

Oort, A. H., and E. R. Ramusson, 1971: Atmospheric circulation statistics. NOAA Prof. Pap. 5, 323 pp. [Available from United States Government Printing Office, Stock No. 0317-0045, c55.25:5.]

Orlanski, I., 1968: Instability of frontal waves. *J. Atmos. Sci.*, **25**, 178–200.

——, and B. B. Ross, 1977: The circulation associated with a cold front. Part I: Dry case. *J. Atmos. Sci.*, **34**, 1619–1633.

——, 1986: Localized baroclinicity: A source for Meso-α cyclones. *J. Atmos. Sci.*, **43**, 2857–2885.

——, J. J. Katzfey, C. Menendez and M. Marino, 1991: Simulation of an extratropical cyclone in the Southern Hemisphere: Model sensitivity. *J. Atmos. Sci.*, in press.

——, ——, M. Marino and C. Menendez, 1989: The role of cyclones in the daily variability of Antarctic ozone. *Proc. Third Int. Conf.*

on *Southern Hemisphere Meteorology and Oceanography,* Boston, Amer. Meteor. Soc., 441 pp.

Pedlosky, J., 1979: *Geophysical Fluid Dynamics.* Springer–Verlag, 709 pp.

Pettersen, S., 1956: *Weather Analysis and Forecasting. Vol 1,* 2nd ed. McGraw-Hill, 428 pp.

Pierrehumbert, R. T., 1984: Local and global baroclinic instability of zonally varying flow. *J. Atmos. Sci.*, **41**, 2141–2162.

Plumb, R. A., 1983: A new look at the energy cycle. *J. Atmos. Sci.*, **40**, 1669–1688.

——, 1985: An alternative form of Andrews conservation law for quasi-geostrophic waves on a steady, nonuniform flow. *J. Atmos. Sci.*, **42**, 298–300.

Randel, W., D. Stevens and J. Stanford, 1987: A study of planetary waves in the southern winter troposphere and stratosphere. Part II: Life cycle. *J. Atmos. Sci.*, **44**, 936–949.

Rossby, C. G., 1945: On the propagation of frequencies and energy in certain types of atmospheric and oceanic waves. *J. Meteor.*, **2**, 187–204.

Sawyer, J. S., 1956: The vertical circulation at meteorological fronts and its relation to frontogenesis. *Proc. Roy. Soc. London,* **A234**, 346–362.

Simmons, A. J., 1972: The nonlinear dynamics of cyclone waves. *J. Atmos. Sci.*, **29**, 38–52.

——, and B. J. Hoskins, 1978: The life cycles of some nonlinear baroclinic waves. *J. Atmos. Sci.*, **35**, 414–432.

——, and ——, 1979: The downstream and upstream development of unstable baroclinic waves. *J. Atmos. Sci.*, **36**, 1239–1254.

——, J. M. Wallace and G. W. Branstator, 1983: Barotropic wave propagation and instability and atmospheric teleconnection patterns. *J. Atmos. Sci.*, **40**, 1363–1392.

Trenberth, K. E., 1981: Observed Southern Hemisphere eddy statistics at 500 mb: Frequency and spatial dependence. *J. Atmos. Sci.*, **38**, 2585–2605.

——, 1986a: The signature of a blocking episode on the general circulation in the Southern Hemisphere. *J. Atmos. Sci.*, **43**, 2061–2069.

——, 1986b: An assessment of the impact of transient eddies on the zonal flow during a blocking episode using localized Eliassen-Palm flux diagnostics. *J. Atmos. Sci.*, **43**, 2070–2087.

Yeh, T.-C., 1949: On energy dispersion in the atmosphere. *J. Meteor.*, **6**, 1–16.